PROPERTIES OF SOLAR MAGNETIC FIELDS FROM SPECKLE POLARIMETRY

Christoph U. Keller

National Solar Observatory, National Optical Astronomy Observatories
P.O.Box 26732
Tucson, AZ 85726-6732, USA
e-mail: ckeller@noao.edu

1 Introduction

Most physical parameters of the solar atmosphere are deduced from spectroscopic observations, which employ spectrographs (resolution $\lambda/\Delta\lambda$ about 500 000) or tunable, narrow-band filters (resolution about 100 000) to record the intensity as a function of two-dimensional spatial location and wavelength. The spectral resolution of such measurements needs to be high enough to resolve the detailed shape of spectral lines.

Spatial structures in the solar photosphere may exist down to scales of the order of the photon mean free path, which is about 70 km in the deep photosphere and corresponds to $0\farcs1$ at disk center. Structures associated with magnetic fields may be expected on even smaller scales. Existing solar telescopes typically have diameters slightly less than a meter. Hence, the scales of solar structures extend out to the diffraction limit of current solar telescopes even in the visible part of the spectrum.

Even though the Sun is a bright object, solar spectroscopic observations with spatial pixel sizes appropriate for diffraction limited resolution are photon limited and require an exposure time of about 1 s to achieve a useful signal to noise ratio (SNR) at the required high spectral and spatial resolution. The photon flux per diffraction limited resolution element is independent of the telescope diameter. Therefore, the spatial resolution of ground-based, spectroscopic solar observations is always degraded by atmospheric distortions (seeing). This limitation is particularly pronounced for solar magnetic field measurements, which are investigated by recording the polarization in spectral lines due to the Zeeman effect. Typically the amount of polarization is only a few percent, which requires longer exposure times than for unpolarized spectroscopic studies.

1.1 High-spatial-resolution solar imaging

Speckle interferometry is an observing and image processing technique that helps to overcome the seeing-induced spatial resolution limit to provide diffraction limited information. Speckle interferometry relies on a number of short exposure measurements (about 0.01 s in the visible part of the spectrum) that are combined in such a way as to preserve the diffraction limited information that is present in the individual exposures, but which is absent in the arithmetically averaged data corresponding to a long-exposure measurement. Speckle interferometry assumes

that the structure of the observed object does not change during the collection of the short-exposure images. Detailed reviews of speckle interferometric methods applied to solar observations can be found in Aime (1989) and von der Lühe (1989).

Short-exposure images in a narrow spectral band contain a limited number of photons. While thousands of images may be collected over periods of hours to achieve a useful SNR in the final reconstruction in night-time applications, this is not applicable to observations of solar structures, which change rapidly with time. The sound speed in the solar photosphere is about 5 km/s and one second of arc corresponds to 725 km at disk center. Therefore, at the diffraction limited resolution of a 50 cm telescope in the visible, the image collection time is limited to 30 s. Otherwise, we need to anticipate artifacts in the speckle reconstructions because the solar surface may have changed its structure during the observing time. Furthermore, most night-time applications of speckle imaging involve the restoration of a set of point sources whose power spectrum is independent of the spatial frequency (when neglecting diffraction at the telescope aperture). In contrast, the power spectrum of typical solar structures shows an exponential decrease with increasing spatial frequency. Therefore, solar speckle interferometry needs a SNR in the short-exposure images that is orders of magnitudes higher than that for typical night-time applications. In conclusion, conventional speckle techniques are hardly able to remove the influence of seeing in two-dimensional spectroscopic observations of the solar surface.

There have been attempts to combine speckle imaging with spectrograph observations. Measurements of the one-dimensional power spectrum of magnetic flux by observing the circular polarization in a Zeeman sensitive line with a rapidly scanning aperture were unsuccessful (Harvey 1986). In contrast, the photospheric brightness-velocity correlation of granulation was determined with high spatial resolution by simultaneously recording the intensity in both wings of a spectral line (Aime et al. 1985). Together with Oskar von der Lühe and Jan Olof Stenflo I have tried to apply conventional speckle imaging to observations recorded through a narrow-band tunable filter in 1988, but the data turned out to be too noisy for successful speckle reconstructions.

A new method to overcome the resolution limit of narrow-band filter images was developed by Keller and von der Lühe (1992a, b). This technique, which I like to call *speckle deconvolution*, provides near-diffraction-limited filtergrams by combining short-exposure images from a narrow and a broad-band channel. When speckle deconvolution is applied to polarization measurements in the wings of a Zeeman sensitive line, the technique is called *speckle polarimetry*. Almost all data shown in this work have been reconstructed with this method. Various results have been reported by Keller (1992, 1993a,b, 1994). Moreover, a method called *speckle spectrography* has recently been developed (Keller & von der Lühe 1994, Keller & Johannesson 1995) that provides near-diffraction-limited slit spectrograph observations.

1.2 Solar magnetic fields

Already the first observations of a magnetic field on the Sun by Hale (1908) showed that the magnetic field in the solar photosphere is highly intermittent. The largest

visible individual elements of the field are represented by the cool, dark sunspots with diameters of 10^4 to 10^5 km, followed by the smaller pores with diameters of 10^3 to 10^4 km and magnetic knots with about 10^3 km in diameter. These magnetic field regions are darker than the average quiet Sun due to the inhibition of convective turn-over in a strong magnetic field (Biermann 1941).

The smallest magnetic field concentrations that form distinct magnetic features are believed to be the *magnetic elements* (Harvey & Livingston 1969), whose diameter is about 10^2 km (diffraction limit of current solar telescopes). Magnetic elements are the basic structures found in plages in active regions and in the network along the boundaries of supergranular cells. It is now widely accepted that the fundamental magnetic structures in these two types of areas are the same. Magnetic elements have a field strength of 1–2 kG in the lower photosphere (Stenflo 1973), which is much larger than the equipartition field strength of a few hundred G. The average internal structure of magnetic elements has been explored by moderate spatial resolution spectrograph data (see Solanki 1993 and Stenflo 1989, 1994 for recent reviews), while high spatial resolution filtergram movies revealed part of their morphology and dynamics (Title et al. 1990, 1992). A few high resolution magnetograms at a resolution of about $0\farcs5$ have been recorded under excellent seeing conditions (e.g., Ramsey et al. 1977, Title et al. 1993), but seeing has prevented the resolution of magnetic elements.

In plages and the network, bright, small structures can be observed. It has often been claimed that these facular and network bright points (henceforth called continuum bright points) are the continuum signatures of magnetic elements (e.g., Mehltretter 1974, Muller 1983, Auffret & Muller 1991). Near disk center the solar filigree, discovered by Dunn and Zirker (1973), consists of strings of tiny bright points seen in the far wing of Hα. The filigrees are also seen in the continuum at a lower contrast though in active regions and their remnants. The individual elements of the filigree are also called *crinkles*, since the filigree is often not just a string of bright dots but shows a crinkled slab-like shape (Dunn & Zirker 1973). This might indicate that there are round points and slab like features, namely the crinkles. The estimated diameters of bright points are near or even below the diffraction limit of present solar telescopes. Regions with filigrees often show *abnormal granulation* (e.g. Dunn & Zirker 1973, Mehltretter 1974, Muller 1985) where there are no regular-size granules but a lot of small-scale structures.

The currently most favored theoretical models of magnetic elements incorporating both bright points and magnetic fields are the so-called solar magnetic *fluxtubes* (see Schüssler 1990 and Steiner 1994 for recent reviews). These fluxtubes appear brighter than the average photosphere since we see deeper and hotter layers in the partly evacuated fluxtube. There exist alternative models (e.g. Schatten & Mayr 1991, Hénoux & Somov 1991), but those models are not able to reproduce the observations as consistently as fluxtubes do.

1.3 Polarimetry

The best diagnostic for magnetic fields on the Sun is the polarization of spectral lines. Polarized light can be described by the four Stokes parameters I (intensity), Q (linear polarization at 0° minus linear polarization at 90°), U (linear polarization

at 45° minus linear polarization at 135°), and V (right circular minus left circular polarization) (e.g., Shurcliff 1962). In the presence of a magnetic field, the Zeeman effect leads to a splitting of spectral lines into several components. These components are circularly polarized in the case of the magnetic field vector being parallel to the line of sight, and linearly polarized in the case of a field perpendicular to the line of sight. The splitting of spectral lines in the visible is most prominent in the large, strong fields of sunspots and pores. In magnetic elements, the splitting is not easily detected in intensity profiles since these tiny features are mostly unresolved. However, the polarization signature in spectral lines is easily measured since the non-magnetic part of the solar atmosphere does not contribute to the polarization signal (with the exception of scattering polarization very close to the solar limb).

Since Stokes V is almost always much larger than Stokes Q and U and the linear polarization is often affected by instrumental effects, solar magnetic fields have mainly been mapped in Stokes V. When Stokes V is normalized with Stokes I, the final product is called *magnetogram*, which roughly corresponds to maps of the longitudinal magnetic flux. Normalizing Stokes V by the continuum intensity I_c leads to very similar results, but V/I_c is easier to interpret.

1.4 Summary

Within the last few years significant progress has been made in our understanding of the small-scale structures of magnetic fields. The current work presents a coherent view of the latest findings obtained by using speckle polarimetric techniques. Sect. 2 introduces the techniques used to reach the diffraction limit in magnetic field maps. After a short review of conventional speckle imaging, speckle deconvolution is discussed in detail and compared to deconvolution from wave-front sensing and adaptive optics. Sect. 3 deals with the optics, real-time frame selection, and data reduction that were employed to obtain the reconstructed images. Results concerning magnetic elements are presented in Sect. 4, while Sect. 5 considers pores. The work concludes with a detailed discussion of the results in Sect. 6.

2 Techniques

2.1 Speckle imaging

Image formation through the turbulent atmosphere of the Earth can be described by the incoherent, space-invariant imaging equation

$$i(t) = o * s(t) \,, \tag{1}$$

where o is the object as seen without the atmosphere, $s(t)$ is the instantaneous point spread function (PSF), which varies in time, and $i(t)$ is the observed image. $*$ is the convolution operator. For the moment I neglect any terms due to noise. Aberrations due to the atmosphere strongly depend on the location of a given source at one moment in time because the telescope beam corresponding to different sources traverses different parts of the atmosphere. If we select a small enough angular extent, the isoplanatic patch, we may assume that the aberrations are the same for all points in this patch. Therefore, the formulation in Eq. (1) is only

correct within an angular area of the size of the the isoplanatic patch, which is typically a few seconds of arc for day-time seeing conditions.

After spatial Fourier transformation of Eq. (1), we obtain

$$I(t) = OS(t) \,, \tag{2}$$

where the upper-case letters represent the Fourier transformed quantities of the corresponding lower-case letters. $S(t)$ is the optical transfer function (OTF); its modulus is the modulation transfer function (MTF). Note that the OTF describes the influence of the atmosphere as well as the diffraction and aberrations due to the telescope. O consists of complex values, which are subsequently split into amplitudes and phases for separate restorations.

The amplitudes of O are usually reconstructed with the Labeyrie (1970) technique. The average power spectrum of the image series is given by

$$\left\langle |I(t)|^2 \right\rangle = |O|^2 \left\langle |S(t)|^2 \right\rangle \,, \tag{3}$$

where the angle brackets denote an ensemble average, i.e. an average over all possible configurations of the Earth's atmosphere. For a sufficiently large number of images, the ensemble average may be approximated by the arithmetic average. In night-time applications, the speckle transfer function, $\langle |S(t)|^2 \rangle$, is determined by observing a point source and calculating the power spectrum of this reference image series. Since the power spectrum of a point source is constant with spatial frequency, the average power spectrum of the reference source is the speckle transfer function.

In the absence of a point source on the Sun, $\langle |S(t)|^2 \rangle$ is determined from model calculations of the Earth's atmosphere using Korff's (1973) approach. There is only a single free parameter in this model speckle transfer function, Fried's (1966) parameter r_0. r_0 corresponds to the diameter of a disk in the aperture of the telescope over which there is no significant wave-front distortion or more accurately, an area over which the rms wave-front distortion equals 1 rad. r_0 can be estimated from the ratio of the power spectrum of the average image and the average of the power spectra of the images. This ratio does not depend on the object (see von der Lühe 1984 for a detailed discussion of the spectral ratio technique). $|O|$ can then be calculated by dividing Eq. (3) by the theoretical speckle transfer function and then taking the square root of this ratio. This procedure is sometimes called amplitude calibration.

The phases of the object, $\Psi(O)$, can be restored with, e.g., the Knox and Thompson (1974) technique. The average cross-spectrum of the image series is defined by

$$\left\langle I(f)\overline{I(f-\delta f)} \right\rangle = O(f)\overline{O(f-\delta f)} \left\langle S(f)\overline{S(f-\delta f)} \right\rangle \,, \tag{4}$$

where δf is a shift vector in the two-dimensional, spatial frequency domain and f indicates the frequency vector. The overbar denotes the complex conjugate quantity. The dependence on time is not written explicitly anymore. As has been realized by Knox and Thompson (1974), $\left\langle S(f)\overline{S(f-\delta f)} \right\rangle$ is a purely real quantity, i.e. its phase is zero. The phase of the average cross-spectrum is therefore

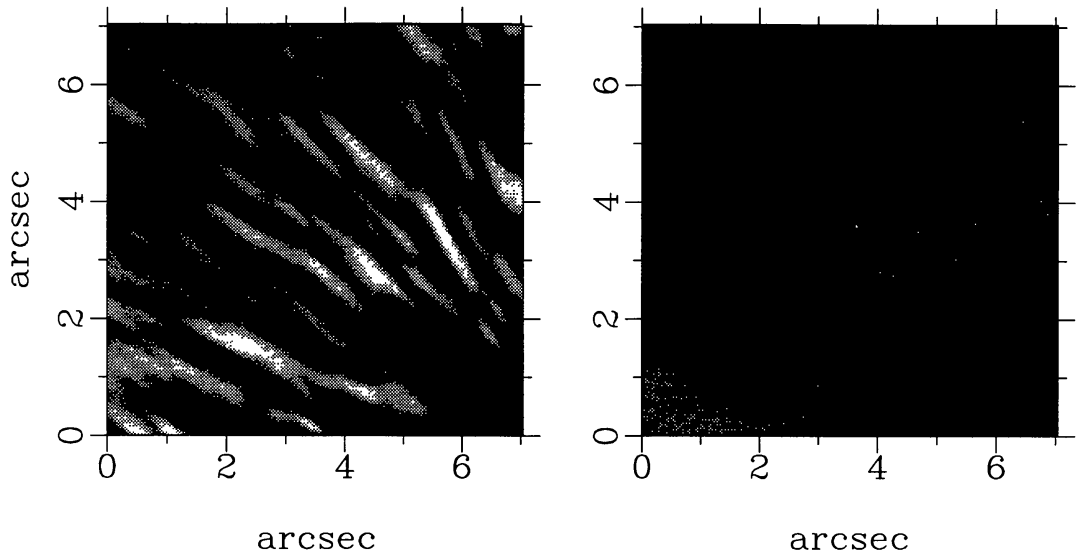

Figure 1: Speckle reconstruction and average image of part of a sunspot penumbra. 200 frames with 1.75 ms exposure time each were recorded at the 1.5-m McMath-Pierce telescope with the Zurich Imaging Stokes Polarimeter I within 30 s. The left panel shows the speckle reconstruction, while the right panel shows the average of these 200 frames. Image motion has been compensated before the images were averaged. Both images are displayed at the same contrast.

equivalent to the phase of the average cross-spectrum of the object alone

$$\Psi(\left\langle I(f)\overline{I(f-\delta f)}\right\rangle) = \Psi(O(f)\overline{O(f-\delta f)})\,, \tag{5}$$

which is proportional to the gradient of $\Psi(O)$

$$\Psi(O(f)\overline{O(f-\delta f)}) = \Psi(O(f)) - \Psi(O(f-\delta f)) \sim \frac{\partial \Psi}{\partial f}\delta f\,. \tag{6}$$

The cross-spectrum is calculated for at least two linearly independent shift vectors δf. Two-dimensional integration of the phase gradient maps restores the true phases of the object O.

After combination of the separately reconstructed amplitudes and phases of the Fourier transform of the object, the true object o is obtained via inverse Fourier transformation. The reconstructions are performed in small, overlapping segments to account for anisoplanatism, i.e. the effect that the field of view is larger than the isoplanatic patch. Therefore the segments have sizes of about the isoplanatic patch diameter (1–2″). After the restoration process the segments are recombined to cover the full field of view. Random noise contributions are compensated for with an appropriate optimum filter (see Brault & White 1971). An optimum filter strongly attenuates Fourier amplitudes whenever they are dominated by noise. A detailed description of the implementation of the above-mentioned techniques has been given by von der Lühe (1992, 1993).

Figure 1 shows the speckle imaging reconstruction and the average image of part of a sunspot penumbra. The gain in spatial resolution is about a factor of

7. The power spectrum of the reconstructed image shows significant amplitudes out to 0.″15. Most results based on speckle imaging concern active regions. Bright points have been investigated by von der Lühe (1994) using the Knox-Thompson technique. While Fourier amplitudes are almost exclusively reconstructed by using the Labeyrie technique, phases may also be reconstructed with the speckle masking technique (Lohmann et al. 1983, Pehlemann & von der Lühe 1989). Speckle masking has the advantage of not being very sensitive to anisoplanatism. However, the computational effort required is enormous. Successful speckle masking reconstructions of the solar granulation and plage areas have been reported by de Boer and Kneer (1992) and de Boer et al. (1992).

The major problem in speckle imaging of solar features is the absence of point sources to calibrate the Fourier amplitudes of the object. Although models of the atmospheric turbulence have been used with good success, it might, however, not always be a sufficiently good approximation of reality. Hence the amplitudes of the speckle reconstruction are limited in accuracy by the restricted reliability of the model of the turbulent atmosphere. Yet another problem is due to telescope aberrations. Their influence is not taken into account when calibrating the Fourier amplitudes of the object, and furthermore, the ensemble average of the the cross-spectrum is not anymore a real quantity. Fortunately, the influence of telescope aberrations on the final restoration is not significant as long as they are much smaller than the distortions induced by the atmosphere, which is often the case.

Both these problems may be circumvented by using a wave-front sensor to directly measure the combined wave-front aberration due to the atmosphere and the telescope. It is not necessary to use a Hartmann-Shack or shearing interferometer wave-front sensor. It is enough to take a few images simultaneously in focus and out of focus. Such a phase diversity approach has been pursued by Löfdahl and Scharmer (1994) and Seldin and Paxman (1994) with considerable success. However, these techniques are still in the process of development and have not yet led to new insights into processes on the solar surface.

2.2 Speckle deconvolution

As we have seen above, conventional speckle imaging cannot be applied to narrow-band images due to insufficient SNR. The basic idea of speckle deconvolution consists in realizing that narrow spectral bands are not required for speckle imaging and that speckle imaging methods are not required for narrow-band imaging. Speckle deconvolution is based on two channels, a broad-band channel ($\approx$ 100 Å full width at half maximum, FWHM) and a narrow-band channel ($\approx$ 0.1 Å FWHM). The broad-band channel is used to determine the instantaneous PSF. The simultaneous narrow-band images are deconvolved with this PSF. Speckle deconvolution is therefore similar to differential speckle imaging (Beckers 1982, Hebden et al. 1986), cross-spectrum techniques (Petrov et al. 1982), and deconvolution from wave-front sensing (Primot et al. 1990). The latter adds a wave-front sensor to measure the instantaneous PSF, which is subsequently used to deconvolve the images.

In the Fourier domain without noise, the equations of image formation in a single isoplanatic patch are given by

$$I_b(t) = O_b S(t), \quad I_n(t) = O_n S(t) \; . \tag{7}$$

The subscripts b and n denote the broad-band and the narrow-band channels, respectively. If the two pass-bands are sufficiently close, we may assume that both channels are subject to the same OTF, $S(t)$. O_b can be determined with conventional speckle imaging since there are enough photons available in the broad-band channel. An estimate O'_n of O_n might then be calculated via

$$O'_n = \left\langle \frac{I_n}{S} \right\rangle = \left\langle \frac{I_n}{I_b} \right\rangle O_b \, . \tag{8}$$

Again I do not write the time dependence explicitly. S has very small values at discrete spatial frequencies resulting in a very noisy instantaneous quotient I_n/S (e.g. Christou et al. 1986). The spatial frequencies at which the amplitudes of S are very small change from one atmospheric realization to the next. Similar to the approaches by Hebden et al. (1986) and Primot et al. (1990), a much better estimate O'_n can be obtained by weighting the quotient I_n/I_b with the power spectrum of i_b:

$$O'_n = \frac{\langle (I_n/I_b)|I_b|^2 \rangle}{\langle |I_b|^2 \rangle} O_b = \frac{\left\langle I_n \overline{I_b} \right\rangle}{\langle |I_b|^2 \rangle} O_b \, . \tag{9}$$

The sum of noisy quotients is replaced by a single, less noisy quotient. Whenever S has very small amplitudes, $|I_b|^2 = |O_b|^2|S|^2$ has even smaller amplitudes. It is easy to show that the approximation as calculated with the weighted average is indeed identical to the true object in the narrow-band channel O_n.

Equation (9) is only valid if $|O_b|^2$ as well as $\langle |S|^2 \rangle$ are finite, since $|I_b|^2 = |O_b|^2|S|^2$. $\langle |S|^2 \rangle$ is always finite within the diffraction limit of the telescope. The object power spectrum $|O_b|^2$ therefore needs to contain power out to the highest frequencies of O_n that should be restored. Already granulation in the quiet Sun fulfills this requirement out to the diffraction limit of almost all current solar telescopes (e.g. von der Lühe 1989).

I now consider the influence of additive random noise, i.e.

$$I_b(t) = O_b S(t) + N_b(t), \quad I_n(t) = O_n S(t) + N_n(t) \, . \tag{10}$$

It is assumed that the noise terms N_n and N_b have zero means (i.e. $\langle N_n \rangle = \langle N_b \rangle = 0$), that they are not correlated with S (e.g. $\langle S N_b \rangle = \langle S \rangle \langle N_b \rangle$), and that N_b and N_n are not correlated (i.e. $\langle N_n N_b \rangle = \langle N_n \rangle \langle N_b \rangle = 0$). Therefore N_n and N_b include the photon noise and any other source of noise (e.g. camera noise) as long as it meets the above mentioned conditions. Photon noise has a Poisson distribution. Hence, the magnitude of the photon noise depends on the intensity. Since the contrast of most of the surface structures on the Sun is low as compared to night-time point sources of different magnitudes, the variation of the magnitude of the photon noise across the image may be neglected. In that case, photon noise is an additive contribution.

Inserting Eq. (10) into Eq. (9) reduces the latter to

$$O'_n = \frac{|O_b|^2 \langle |S|^2 \rangle}{|O_b|^2 \langle |S|^2 \rangle + \langle |N_b|^2 \rangle} O_n = \Phi O_n \, , \tag{11}$$

where Φ has the form of an optimum filter (see Brault & White 1971). When the noise power dominates over the object power spectrum, the filter Φ tends towards

Table 1: Comparison of high spatial resolution techniques for narrow-band imaging of the Sun.

	speckle deconvolution	deconvolution from wave-front sensing	adaptive optics
measurement	broad-band	broad-band	white-light
wave-front sensing	broad-band	white-light	white-light
field of view	arbitrary	few isoplanatic patches	one isoplanatic patch
data processing	large	moderate	none
optical complexity	low	moderate	high
costs	low	moderate	high

zero. This Fourier filtering effect may be corrected for by determining an estimate of $\langle |N_b|^2 \rangle$ via the average power spectrum of an out-of-focus image series in the broad-band channel. In practice, the relative noise in the narrow-band channel is always larger than in the broad-band channel, i.e. the power in the broad-band channel stays above the noise power spectrum out to higher frequencies than the narrow-band channel. Therefore the Fourier filtering effect may be neglected except for the case when extremely accurate power spectrum estimates in the narrow-band channel are required. A detailed description of speckle deconvolution and further discussions of the influence of noise may be found in Keller and von der Lühe (1992b).

Since the broad- and narrow-band channels are detected with separate cameras or at least separate detector areas, the problem of accurately matching the two images could arise. However, close examination of Eq. (9) reveals that shifts between the two images much smaller than the isoplanatic patch size do not have an influence on the deconvolution. The achieved accuracy in correcting for the shift is about 10% of the diameter of the diffraction-limited resolution element.

The SNR of the reconstructed narrow-band channel is approximately given by the geometric mean of the SNR in the two channels (Petrov et al. 1986). This explains the major improvement of speckle deconvolution over direct speckle imaging in the narrow-band channel. The SNR in the broad-band channel may easily be a factor of 100 larger than in the narrow-band channel. Then the speckle deconvolution reconstruction has a factor of 10 better SNR than the direct speckle imaging approach.

Speckle deconvolution, deconvolution from wave-front sensing, and adaptive optics are compared in Table 1, which is similar to the table given in Fontanella and Primot (1987). Broad-band implies filter pass-bands of about 10 nm, while white-light indicates several 100 nm. Speckle deconvolution has the large advantage that it can be carried out with existing equipment and that arbitrarily large fields of view can be reconstructed. On the other hand, a large computational effort is required to obtain the reconstructions.

Another problem of speckle imaging is the variation of the size of the isoplanatic patch with spatial frequency in the images. For instance, image motion is correlated over larger spatial scales than higher-order aberrations. The speckle reconstruction is applied to small segments only that have about the size of the isoplanatic patch.

However, the segment size does not depend on the spatial frequencies of the reconstructions. A promising approach might be the application of wavelet transforms (e.g. Morlet et al. 1982; Daubechies 1988), which are similar to a series of windowed Fourier transforms. The window size of wavelets generally decreases with increasing frequency and the windows for a particular frequency cover the spatial domain. A possible drawback might be that the Labeyrie and the Knox-Thompson techniques are much more complicated to formulate in the wavelet domain as compared with the Fourier domain because no standard mathematical operation has a particularly simple representation in the wavelet domain (Press 1991). Nevertheless the wavelet transform seems very promising to attack the problem of the frequency dependence of the isoplanatic patch size. Furthermore, the wavelet transform approach would also take into account the segmentation of a large field of view in a natural way.

3 Observations

The data on which the current results are based have been recorded at the 50 cm Swedish Vacuum Solar Telescope at La Palma (Canary Islands) in October 1990. The excellent seeing at La Palma combined with the high optical quality of the telescope and the availability of fast CCD cameras coupled with a powerful image processing system rendered that observatory an ideal place for the first application of speckle polarimetry. In the following paragraphs I will discuss the optical setup, the data acquisition, and the data reduction.

3.1 Optics

Circular polarization was detected by having the light beam coming from the telescope pass through a quarter-wave plate, which converts circular to linear polarization (see Fig. 2 for a schematic view of the optical setup). A double-calcite beam-splitter then gave rise to two beams that are orthogonally polarized and, due to the quarter-wave plate, correspond to left and right circularly polarized light, respectively. By using two calcites instead of one, it is assured that both beams have equal optical path lengths. The spatial separation of the two beams was chosen such that both beams could be collected with a single camera. Subtraction of the two beams results in an image of Stokes V. Since some of the subsequent optical elements were sensitive to linear polarization, another quarter-wave plate was put behind the calcite beam-splitter. By rotating the quarter-wave plate, the average transmission in the two beams could be equalized despite the polarization sensitivity of the subsequent beam-splitter and the tunable filter.

The two circularly polarized beams were subsequently separated into two channels by a beam-splitter cube. The first channel, the broad-band channel, passed through a 8.2 nm full width at half maximum (FWHM) interference filter centered at 520 nm and a neutral density filter to avoid saturation of the detector. The light was detected with a COHU 6500 CCD video camera. The second, narrow-band channel passed through a Zeiss tunable filter (see Lundstedt et al. 1991 for details) with a FWHM of 0.015 nm. It was detected by a second CCD video camera of the same type as the first one. The image scale amounted to $0\farcs063$ by $0\farcs087$ per pixel. With a diffraction limited resolution of $0\farcs22$ at 525 nm, the images are spa-

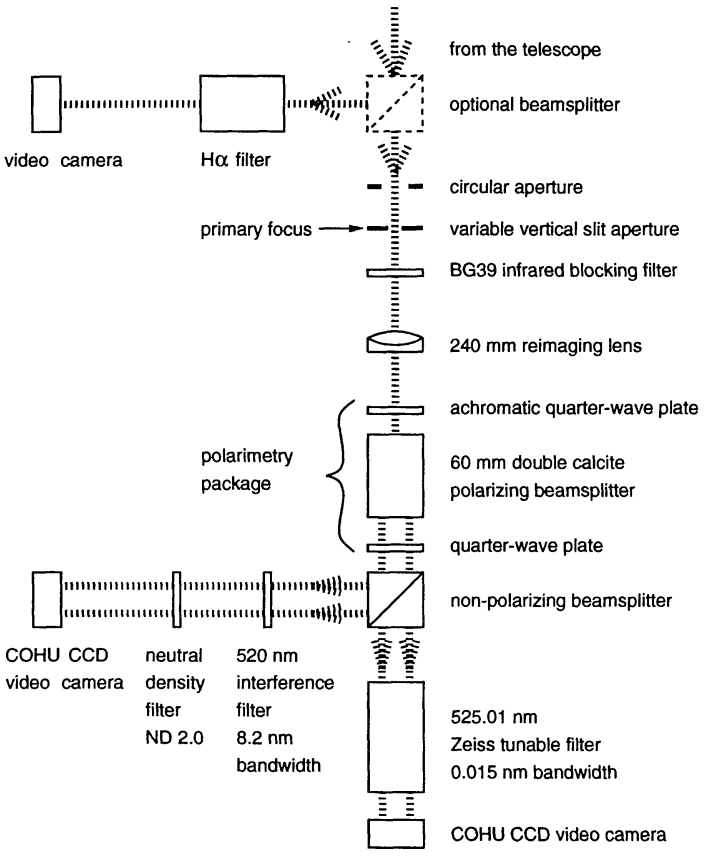

Figure 2: Schematic of the optical setup that was used for speckle polarimetric imaging at the Swedish Vacuum Solar Telescope at La Palma. The optical elements and their separations are not drawn to scale.

tially oversampled. This avoids aliasing, i.e. mapping of high spatial frequencies into lower frequency ranges, reduces the influence of the detector MTF due to its discrete pixel structure, and improves the SNR for a given spatial frequency, but reduces the field of view.

All the optical elements had a quality of a tenth of a wave. The optics, which were not common to the two channels, should not produce significant differential aberrations. Otherwise spurious signals might appear when applying the speckle deconvolution technique to the two channels. The similarity of the two channels was verified by placing a USAF three-bar target slide in the primary focus and comparing the images taken with the two cameras. Neither the difference image nor the amplitude and phase spectra of the two channels show a significant difference out to the diffraction limit of the telescope.

The double calcite beam-splitter leads to differential aberration between the two polarization states, which may lead to artificial Stokes V signals when subtracting the two images. Furthermore, aberrations due to the Zeiss tunable filter might be different in the two beams since they pass through different parts of the filter. Again, the observed amplitude and phase spectra of images of the three-bar target slide show the two beams to be identical out to the diffraction limit of the telescope. I conclude that differential aberrations due to the beam-splitter or the Zeiss filter are not significant. This is in agreement with the theoretical expectations (Semel 1987) for this particular set-up which yield an astigmatism of $0\farcs05$ due to the double-calcite beam-splitter. Spatial stray-light produced by the optics behind the

prime focus of the telescope has been measured in the dark parts of the target slide image and amounts to 1%, which may be neglected.

The line used with this setup was the Fe I 525.02 nm line, which has a Landé g-factor of 3. Therefore it is highly sensitive to magnetic fields. However, the Stokes V amplitude of this line is weakened by the enhanced temperatures in magnetic elements. Furthermore, blends appearing in sunspot spectra make its use rather doubtful in sunspots. In fact, it was not the line of choice, but a problem with the tunable filter forced us to use this line. Since the Stokes V signal is roughly proportional to the derivative of the Stokes I spectrum with respect to wavelength, it is strongest in the wings of a spectral line. The blue wing of Fe I 525.02 nm was selected because it tends to be stronger than the red wing in magnetic elements close to disk center (e.g. Stenflo et al. 1984).

3.2 Data acquisition

The two video cameras were synchronized with respect to each other and generated 60 frames per second. The effective exposure time was 16 ms. A real-time frame selection system developed by W. Wang and G. Scharmer stored the 150 sharpest images acquired within 30 s or 60 s. The frame sharpness was determined by an analogue video circuit that measured the power in a certain temporal frequency band. This operation is equivalent to determining the average power spectrum in the single images within a certain spatial frequency range. If the band-pass is appropriately chosen, i.e. by avoiding the lowest frequencies that are not affected by seeing and the highest frequencies that are dominated by noise, a sharpness value can be determined that is closely related to the seeing quality in a single exposure. The sharpness of an incoming image is then compared to the sharpness of all images already stored in the image acquisition system. If the new image has a sharpness that is better than the worst image already stored, the latter is replaced with the new image. Else, the new image is discarded. The image acquisition system was limited in storage to 150 frames for each of the two cameras.

The frame selection technique delivers a narrow distribution of the Fried parameter r_0 in the image series. This is very advantageous for speckle interferometry since it eliminates binning of the speckle data into bins of equal r_0, and hence allows us to calibrate the amplitudes with a single value of r_0 instead of a complicated distribution. The selection of the 10% sharpest frames results in an improvement of the average r_0 by a factor of 2 to 3 (Beckers 1989).

Each frame had a size of 200 by 240 pixels at a depth of 8 bits. After the sequence had been recorded in the memory of the image acquisition system, the images were transferred to hard disk, which took about 5 to 8 minutes. Therefore, it was not possible to obtain sequences of reconstructions that were close enough in time to follow the evolution of magnetic elements.

3.3 Data reduction

The raw images were carefully corrected for dark current and pixel-to-pixel gain variations. Out of the 150 image pairs, about 100 were selected that did not show any artifacts due to problems with the image acquisition system. Only one of the two beams in the broad-band channel was used for further analysis. The two

beams in the narrow-band channel corresponding to the two polarization states were subtracted from each other to obtain a series of Stokes V images. The sum of the two beams gives the Stokes I images. Since the equation of image formation is linear, a difference or sum between two simultaneous images may be reconstructed in the same way as a regular image is restored. Furthermore, the atmosphere is not birefringent, which leads to both polarization states having the same OTF. The thus prepared three image series (broad-band images, Stokes I and Stokes V in the wing of the line) are reconstructed with the speckle program. In the following we often refer to images recorded in the broad-band channel as the continuum. Spectral lines also contribute to the signal in the broad-band channel, but their contribution is only a few percent. I do not show any Stokes I images because they strongly resemble the continuum images and do not shed more light on the magnetic field structures.

The images are reconstructed with an improved version of von der Lühe's KISIP program (1993), which uses Labeyrie's technique to reconstruct the amplitudes and the Knox Thompson algorithm to recover the phases. This speckle imaging code corrects for the combined OTF of the telescope and the atmosphere, but it does not take into account the MTF of the detector. Owing to the oversampling, the detector MTF is still at 80% at the diffraction limit of the telescope. I therefore neglect the influence of the detector MTF. The main changes with respect to the original KISIP program consisted in adding code to perform speckle deconvolution, to allow non-square images, and to use a weighted phase-integration method when reconstructing the phases of the object. Since the speckle reconstruction also corrects for the diffraction of the telescope, the effective PSF of the reconstruction is closer to a sinc than to an Airy function or a Gaussian. This leads to a certain amount of ringing, but this is a problem with any method that tries to correct for the telescope MTF.

Keller and von der Lühe (1992b) used a Fourier filter to remove noise in the Stokes V images. That filter assumes that the SNR in the Stokes V images is constant across the images. While the noise is almost constant across the image, the Stokes V signal has a large dynamic range due to the intermittence of solar magnetic fields. This leads to a strong smoothing of isolated magnetic signals. To avoid this problem, most of the Stokes V data shown in the following are smoothed with a 3-by-3-pixel median filter to remove noise spikes. Furthermore, the sign of Stokes V has always been adjusted so that the dominating magnetic polarity shows positive Stokes V signals because solid contour lines are easier to recognize than dashed lines produced by the image processing system.

The present results strongly depend on the reliability of the speckle restoration. Its reliability was estimated by restoring two independent data sets extracted from the same image series. The broad-band channel reconstructions differ on average by about 0.5% and the Stokes V/I_c images by 1%. The reality of the features shown in the next sections has always been confirmed by their presence in unrestored, average Stokes V images. The spatial resolution in the broad-band channel often reaches close to the diffraction limit, while that of Stokes V/I_c is at least $0\farcs3$. In the best seeing conditions, the FWHM of the PSF reaches 140 km.

4 Magnetic elements

4.1 Magnetic elements close to disk center

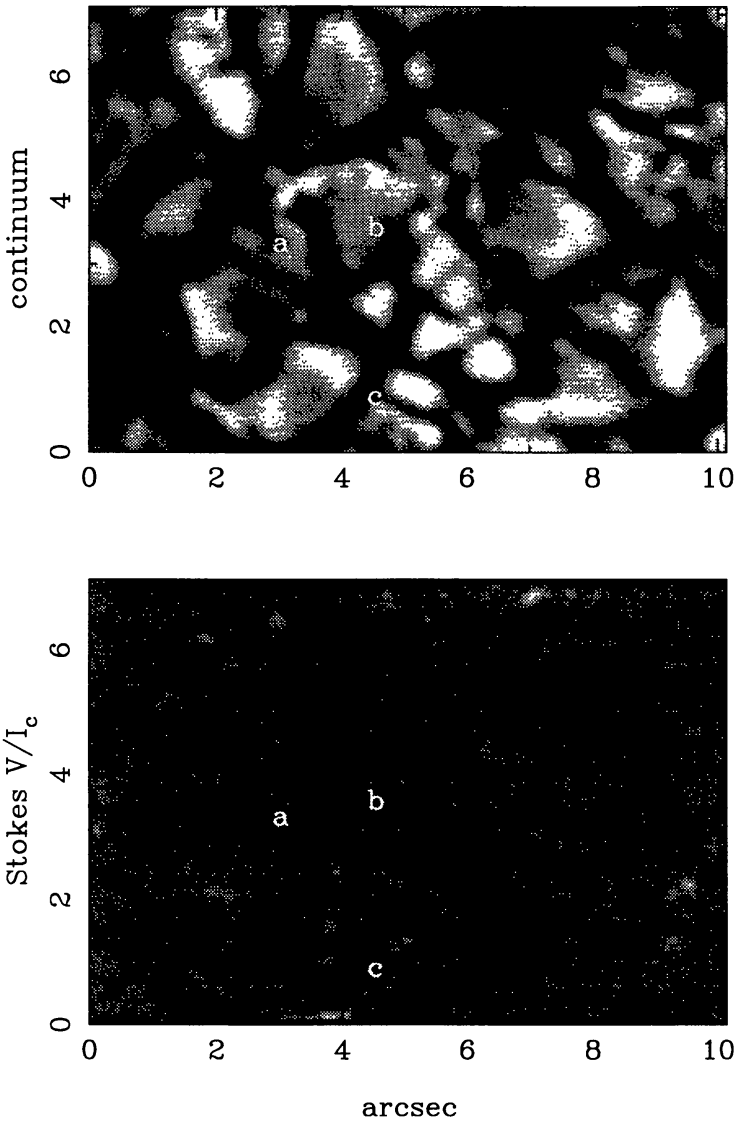

Figure 3: The continuum image (upper panel) and the Stokes V/I_c signal (lower panel) of solar magnetic elements in quiet granulation near a weak plage close to disk center. Above the points labeled "a" and "b" small magnetic elements can be seen that are associated with concentrated magnetic fields. To the right of "c" there are small, very bright granules that are not associated with a magnetic signal.

Figure 3 shows continuum bright points in the quiet granulation near a weak plage. The daisy-like granules surrounding point "a" are typical for network bright points (Muller et al. 1989). The continuum contrast (relative deviation from the average intensity) is 34%. Bright points also appear along granule borders above "b". These points coincide with a concentrated Stokes V/I_c signal of up to 4%. Since these magnetic elements are probably not yet resolved (for a resolved fluxtube I would expect a peak Stokes V/I_c signal of about 10%), the continuum contrast given above is only a lower limit. Unfortunately this is the only observation of magnetic elements outside of plages. However, many network magnetic elements have recently been observed with speckle polarimetric methods, which will give statistically significant answers on network fluxtubes. The data still need to be analyzed.

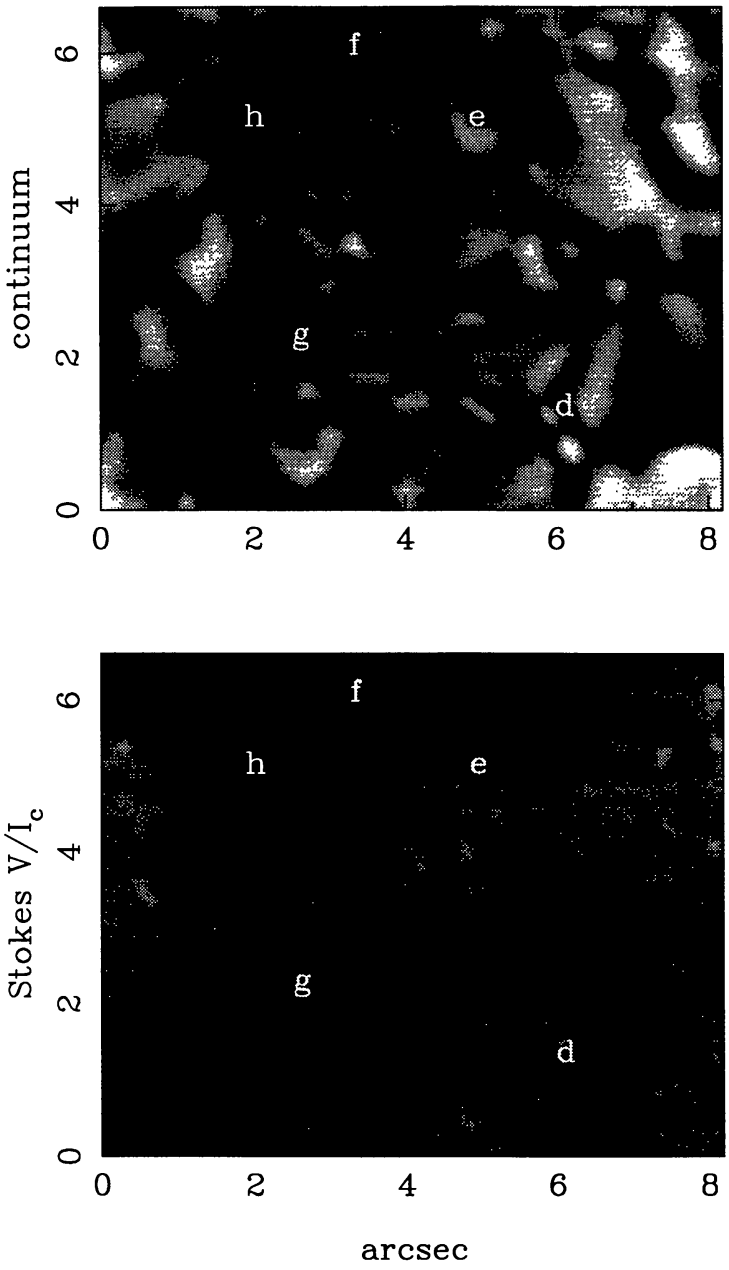

Figure 4: The same as Fig. 3 in a pore region close to disk center. The grey scale of the lower panel is different from Fig. 3 to account for the larger Stokes V/I_c signals here. The bright point labeled "d" is an almost fully resolved magnetic element with a FWHM of 180 km. Another, much larger element can be seen above "e" and "f". "g" indicates a region that is highly magnetic with many small-scale features. "h" is a pore.

A nearly resolved magnetic element in a strong plage can be seen in Fig. 4 (element "d"). The maximum Stokes V/I_c signal there is 8% and the continuum contrast is 32%. An empirical plage fluxtube model with 2360 G at $\tau_{5000} = 1$ (Keller et al. 1990) exhibits a maximum Stokes V/I_c signal of 10% when the simulated Stokes V profile is convolved with the measured tunable filter profile and the axis of the fluxtube is assumed to be parallel to the line of sight. The latter is a reasonable assumption since the observations have been performed close to disk center and the magnetic field in fluxtubes is roughly vertical. The same model also reproduces the 30% continuum contrast. Because the observed maximum polarization is so close to the theoretically expected maximum Stokes V/I_c signal, the magnetic field structure must be almost spatially resolved. The observed FWHM is 180 km in

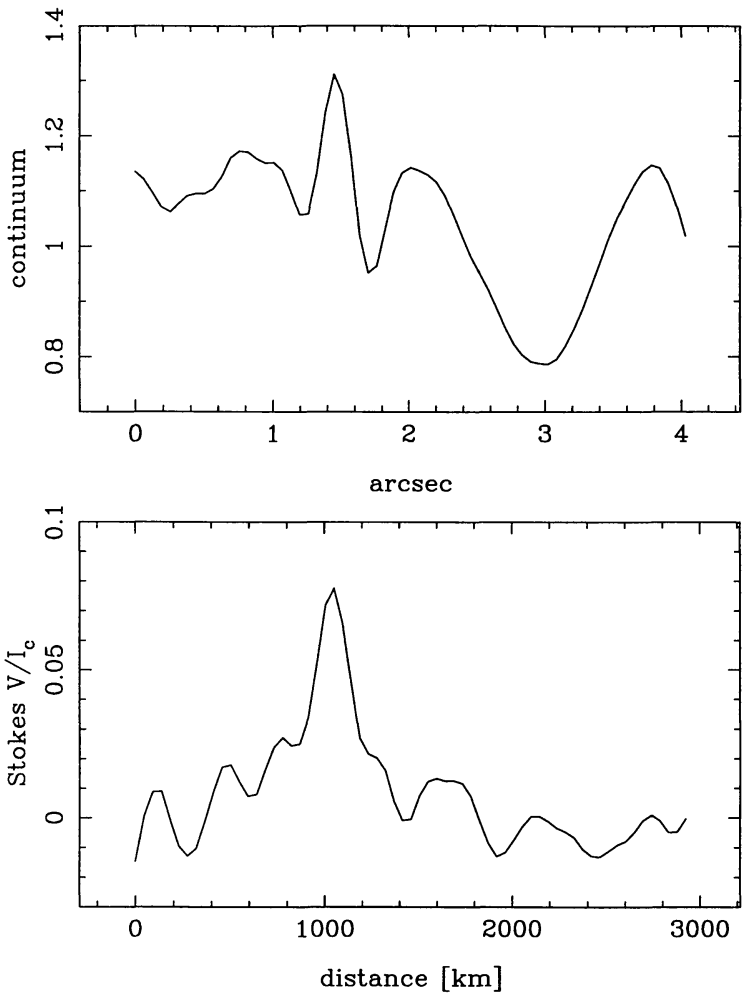

Figure 5: A cut through the magnetic element "d" in Fig. 4. The upper panel shows the continuum brightness where 1.0 corresponds to the average brightness. The lower panel shows the Stokes V/I_c signal. Scales are given both in arcseconds and km. The strong magnetic signal is cospatial with the brightness enhancement.

Stokes V/I_c as well as in the continuum image when taking into account the local background signal (see Fig. 5, which shows cuts across the structure). The sizeable continuum contrast and the large, concentrated polarization signal indicate that this feature is indeed a fluxtube as expected by theoretical models. Although the fluxtube is nearly resolved, the bright structure seen in the continuum might still be well below the resolution limit and the true continuum contrast might be larger than 30%. However, this requires that the brightness structure and the magnetic field are not cospatial anymore. The magnetic flux is about 6×10^{17} Mx.

The lifetime of the concentrated state is probably shorter than 16 minutes. Figure 6 shows part of the region along with the same location about 8 minutes before and after the data for Fig. 4 have been recorded. Along with the continuum images the average Stokes V images are shown, i.e. not reconstructed with the speckle deconvolution technique. The averages have been obtained by correcting each image for image motion and then taking an arithmetic average over all images in the series. Showing the average Stokes V signal has the advantage that artifacts due to the speckle reconstruction are not relevant. The seeing conditions were excellent in all three image sequences, the last series having slightly better conditions than the first two. The first image pair shows a small, slightly fuzzy bright point at the same location, but there is no cospatial magnetogram signal.

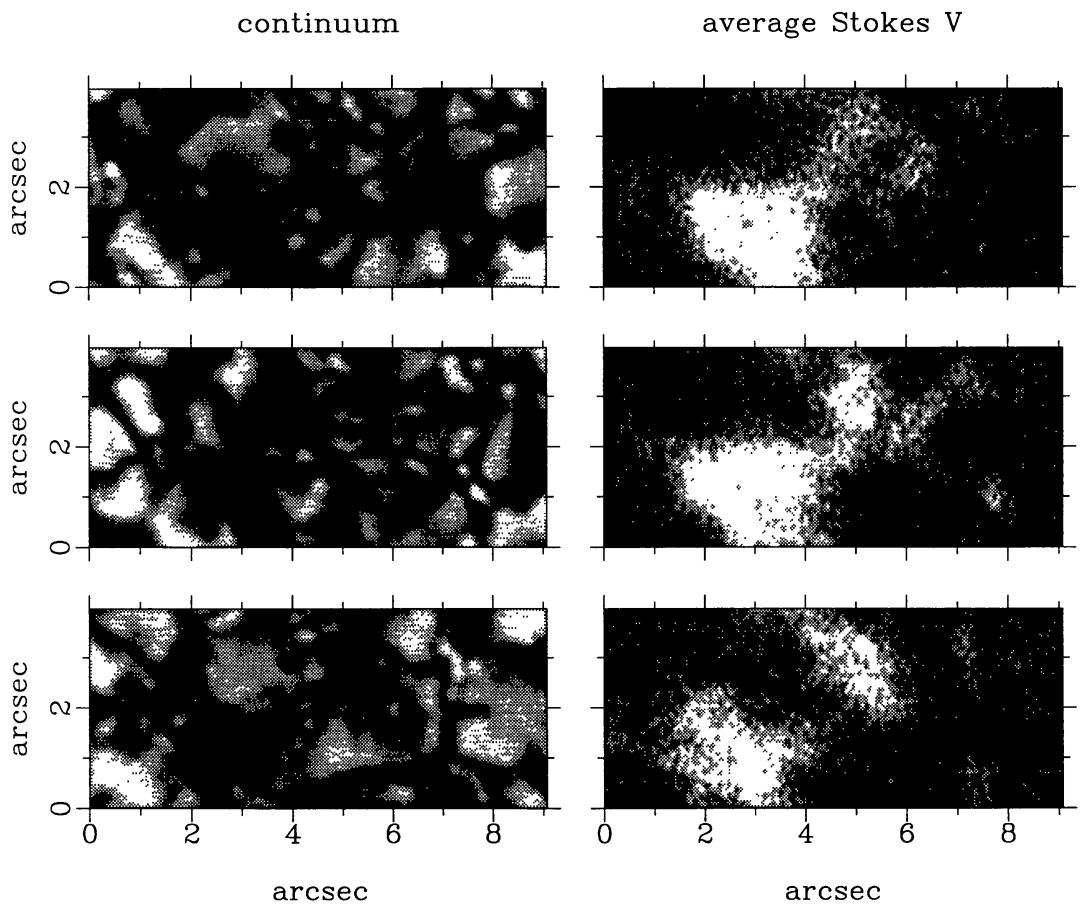

Figure 6: A time sequence of the region where the fluxtube appeared. Time increases from top to bottom and the time difference between subsequent restorations is about 8 minutes. The left panels show the restored continuum images, while the right panels show the average, unrestored Stokes V images. The bright fluxtube shows up in the lower right corner of the center panels. Note that 8 minutes before and after the center images have been recorded, the magnetic flux at the same place is hardly detectable. Fried's parameter r_0 varied between 15 cm and 18 cm, which corresponds to excellent seeing for all three time steps.

The next time step shows the familiar bright point along with the concentrated magnetic signal. Note that even in the average, unreconstructed Stokes V image the signal is concentrated and well above the noise level. The subsequent time step shows a small-scale elongated structure at about the same place. A fuzzy magnetic signal is visible, although shifted towards the bottom of the frame. The speckle reconstruction of the last time step also does not show a concentrated Stokes V signal. It is interesting to note that the region as seen at this high spatial resolution changes drastically on the small scales within short periods of time. Not only do small bright and dark structures change within a few minutes, also the shape of the pore changes significantly. The location of magnetic fields are, however, more stable.

Let us look at some more features in Fig. 4. The dark magnetic structure just

above "e" with a continuum contrast of −31% has a maximum polarization of 12% and measures about 300 by 1500 km in size. When accounting for the temperature sensitivity of the Fe I 525.02 nm spectral line, this polarization is also consistent with a fully resolved magnetic field. The magnetic signal extends to the upper left (label "f") without a cospatial dark structure. Although the magnetic field to the right of and below of "g" seems to be concentrated in individual elements, there is no particular continuum signature that is exactly cospatial with the magnetic signal. Some dark, dot-like structures may be recognized in that region together with small-scale bright structures. The average continuum contrast in that region is −6%. About 50% of the area is covered with strong magnetic fields if I assume that the field strength is about 2 kG at the level of continuum formation.

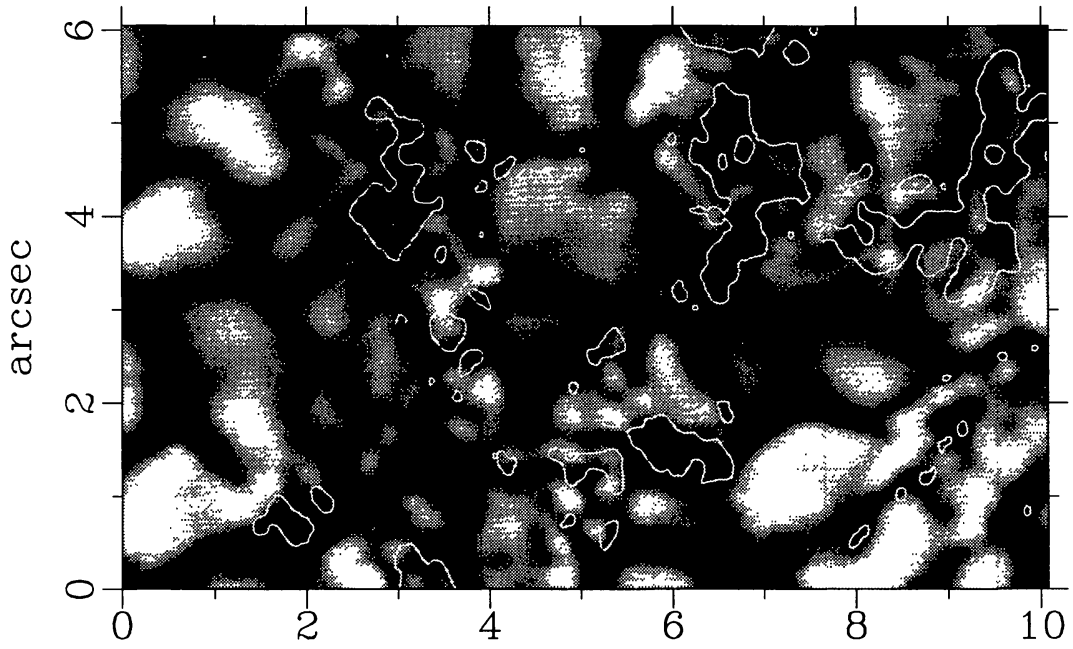

Figure 7: A unipolar plage region close to disk center at $\mu = 0.94$. The contour lines are drawn at a Stokes V/I_c signal level of 4%. They outline significant flux concentrations. The magnetic signal mostly appears in regions that are darker than the average continuum brightness. Some signals are associated with bright structures. A magnetic signal never appears in a structure that looks like a regular granule.

Figures 3 and 4 show rare cases of bright points cospatial with concentrated magnetic signals. Indeed, these are the only cases close to disk center that I have seen so far. It is therefore not a common feature as seen with the present spatial resolution. Figures 7 and 8 show plages without pores, i.e. weaker plages as compared to Fig. 4 at $\mu = 0.94$, i.e. still close to disk center. $\mu = \cos\theta$ and θ is the heliocentric angle. The contour lines indicate a specific Stokes V/I_c signal. Regions within the contour lines are likely to correspond to highly concentrated magnetic fields. Only a single contour line is drawn to limit the amount of information in the figures. Dotted lines correspond to the opposite polarity. The typical structure of abnormal granulation is visible close to the magnetic field regions.

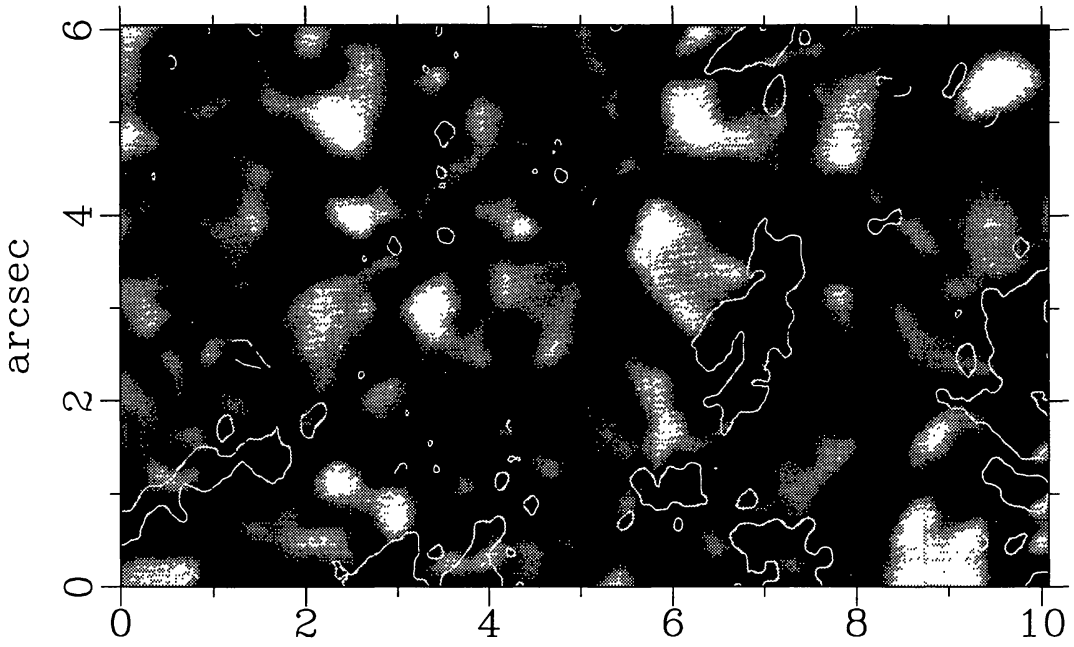

Figure 8: Another plage region close to disk center at $\mu = 0.94$. The contour lines are drawn at a Stokes V/I_c signal level of 4% to show the location of significant flux concentrations. The smallest elements might be due to noise.

There is, however, no clear and detailed relation between magnetic field structure and continuum brightness. There certainly are structures that are associated with structures brighter than the average quiet Sun brightness and there are elements that are associated with darker structures. In fact, it is impossible to know the exact location of a magnetic element by just looking at the brightness distribution. In general, there are discrete magnetic elements of varying size that are almost always located in regions that cannot be identified as normal granulation.

As mentioned in the introduction, bright structures, which are sometimes elongated, have been seen in magnetic areas. A thin (about $0\farcs2$), long (about $2\farcs5$) brightness structure is shown in Fig. 9. While the brightness along the structure does not show a clumpy behavior, the magnetic signal seems to be concentrated into more or less individual elements that are even not cospatial with the brightness structure. Unfortunately, this is the only such case seen in the reconstructions. Again, the brightness structure is no proxy of the magnetic field location, although strange brightness structures are often associated with magnetic fields.

4.2 Faculae close to the limb

While the brightness structure of magnetic fields close to disk center is still a matter of discussion, it is well known that bright structures close to the solar limb are associated with magnetic fields. These faculae have been extensively studied in the past, but high-resolution, simultaneous magnetic field measurements were lacking. The exact relationship between faculae and magnetic elements was not clear. Figures 10 and 11 show faculae at $\mu = 0.43$, which is about $90''$ from the solar limb. The contour lines are drawn at a Stokes V/I_c signal that corresponds

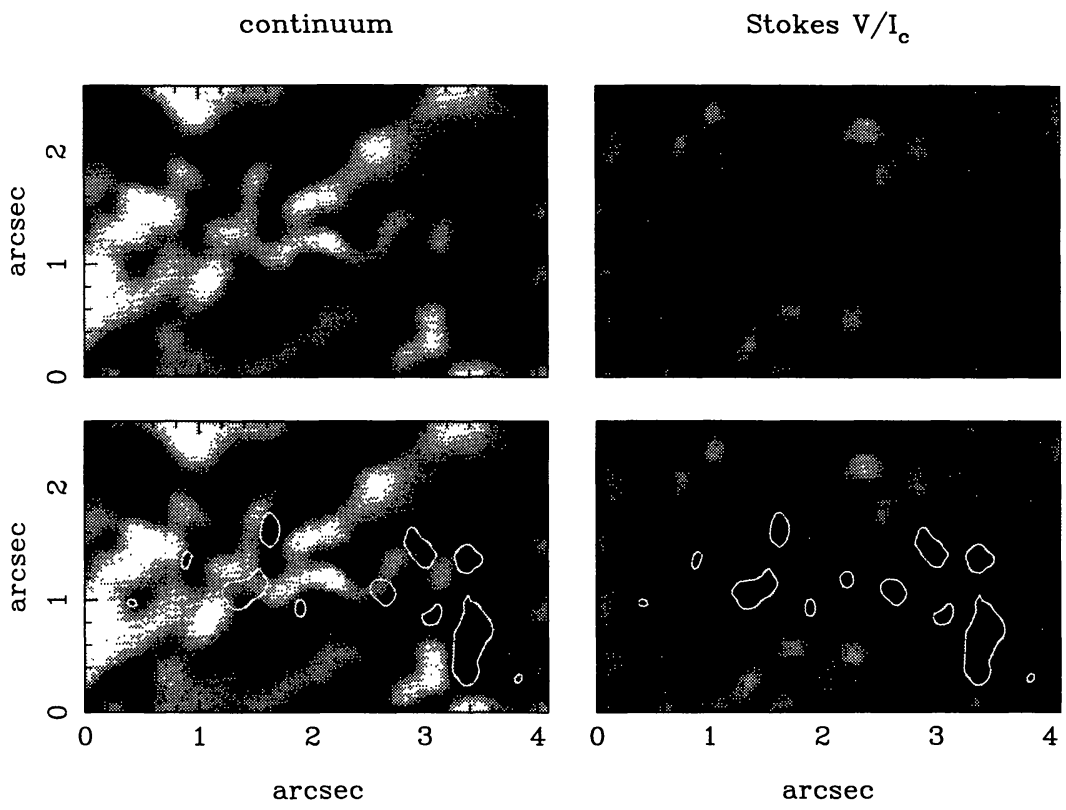

Figure 9: A crinkle close to disk center and the associated magnetic signature. The continuum image has black and white corresponding to 0.75 and 1.3 times the average brightness while for the Stokes V/I_c signal black and white correspond to $\pm 5.5\%$. The lower two panels have 4% V/I_c signal contour lines overlaid.

to a filling factor of roughly 50% in the case of a strong-field fluxtube. Magnetic elements are associated with bright, point-like features. Very bright points are almost always located in magnetic field regions. Nevertheless, there is certainly no one-to-one relation between brightness structures and magnetic fields. Due to foreshortening, the morphology of the granulation is harder to recognize. Some of the magnetic elements seem to be associated with the borders of granules while others are not connected with granules.

Scatter plots in Fig. 12 show the relation between continuum brightness and Stokes V/I_c signal in a more quantitative fashion. The upper panel corresponds to the plage region shown in Fig. 7 and the lower panel corresponds to the facular region shown in Fig. 10. Every point in the plots corresponds to a single pixel pair in the images. The brightness in both images was normalized such that the average brightness corresponds to 1.0. Close to disk center the pixels with the strongest V/I_c signal have a brightness that is about 15% darker than the average. Pixels with lower magnetic signals may be brighter or darker than the average and do not show a significantly different brightness distribution as compared to non-magnetic pixels. The brightness of the pixels with the largest polarization signal are not darker than dark regions in non-magnetic regions. In contrast, close to the limb, there seems to be a relatively linear relationship between Stokes V/I_c signal and

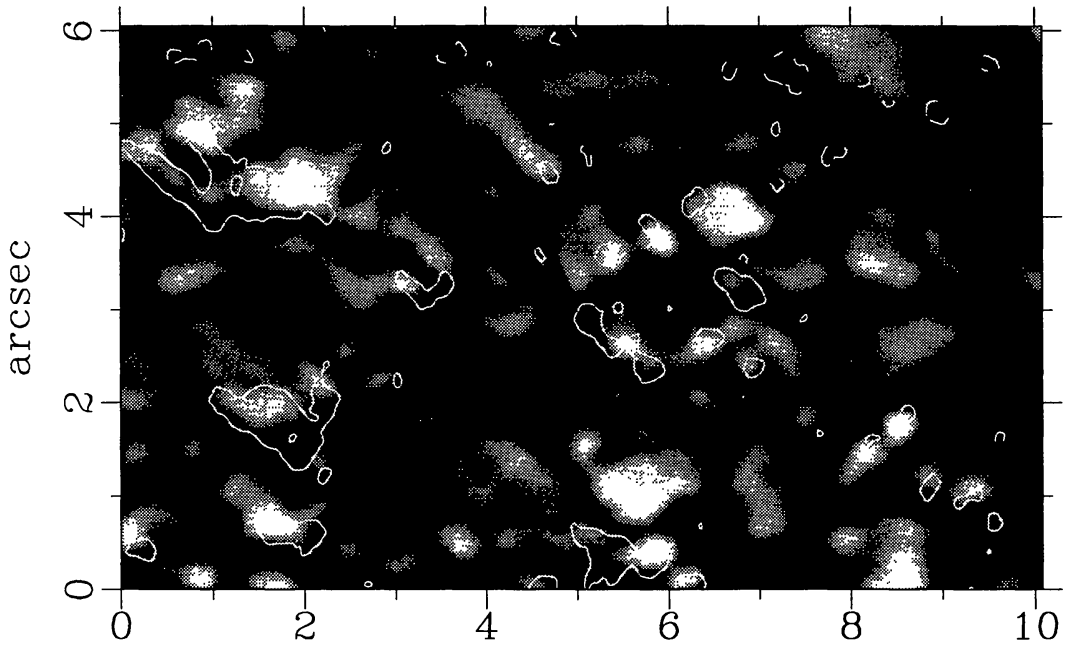

Figure 10: Faculae near the limb at $\mu = 0.43$. There is a good correlation between brightness and Stokes V/I_c signal although magnetic regions without significant brightness enhancement exist. Contour lines are drawn at V/I_c signal level of 3%. This is less than typically shown at disk center because the angle between the line of sight and the magnetic field vector leads to a reduction of the Stokes V signal. Opposite polarity features are indicated with dashed contour lines.

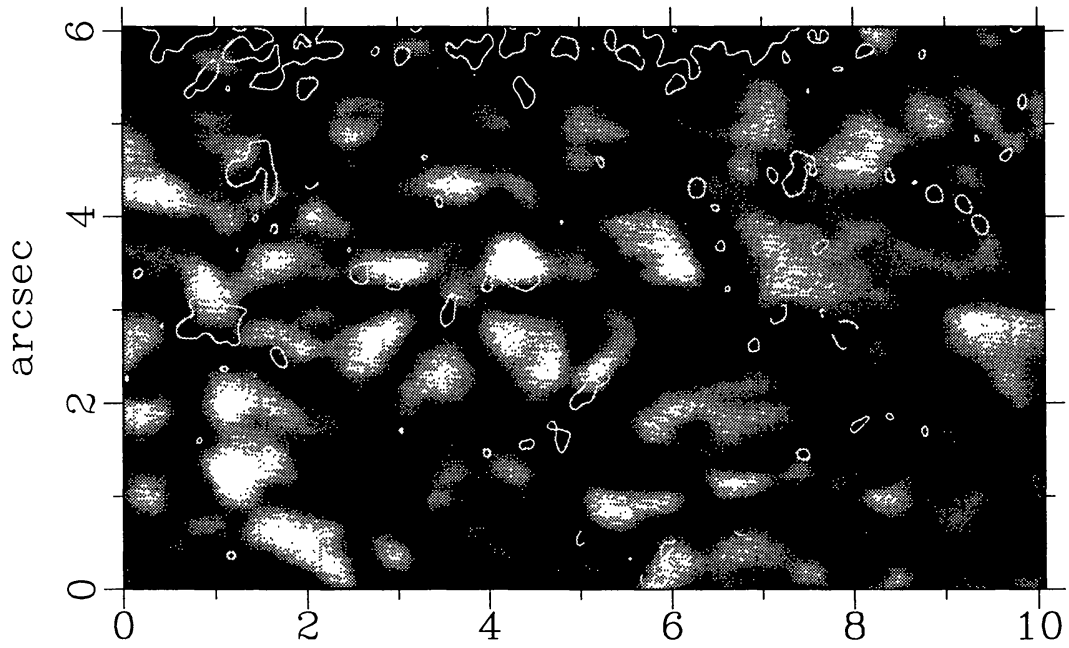

Figure 11: Faculae near the limb at $\mu = 0.43$ in another region than shown in Fig. 10. A sunspot penumbra is located just above the field of view.

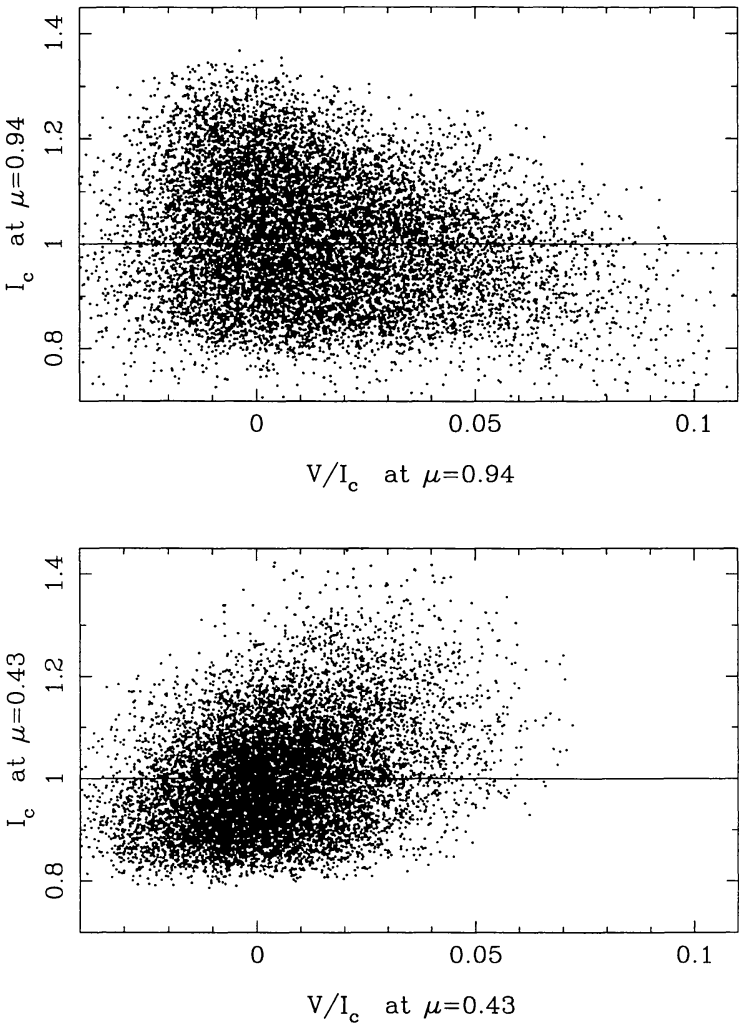

Figure 12: Relation between Stokes V/I_c and continuum intensity I_c. Close to disk center the strongest magnetic signals tend to occur in locations that are darker than the average brightness, while close to the limb the strongest magnetic signals are almost exclusively in areas that are brighter than the average image.

brightness, and the highest contrast is only reached in magnetic pixels.

4.3 Non-magnetic bright points

It has been suggested by several authors that bright points are the continuum signatures of magnetic elements. A counter-example is shown in Fig. 13, which has been extracted from the penumbra movie of Frank et al. (1991). These images have not been reconstructed with speckle imaging and deconvolution, but they have been recorded during spectacular seeing conditions through the Zeiss filter in the Fe I line at 525.02 nm with effective exposure times of about one second. A bright point without significant cospatial magnetogram signal can be seen in an area of 4″ by 4″ during a period of 20 min. The penumbra of a major sunspot in the mature bipolar active region NOAA 6337 (heliocentric distance 24°) is just to the left of the field of view. The point is moving away from the active region. The sensitivity in the magnetograms is about 1×10^{16} Mx per 0.″2 by 0.″2 resolution element. The lifetime of the bright point is longer than 20 minutes and the horizontal velocity is about 1–1.5 km/s. This fast moving point has all the characteristics of network bright points in the moving phase described by Choudhuri et al. (1993). Although this

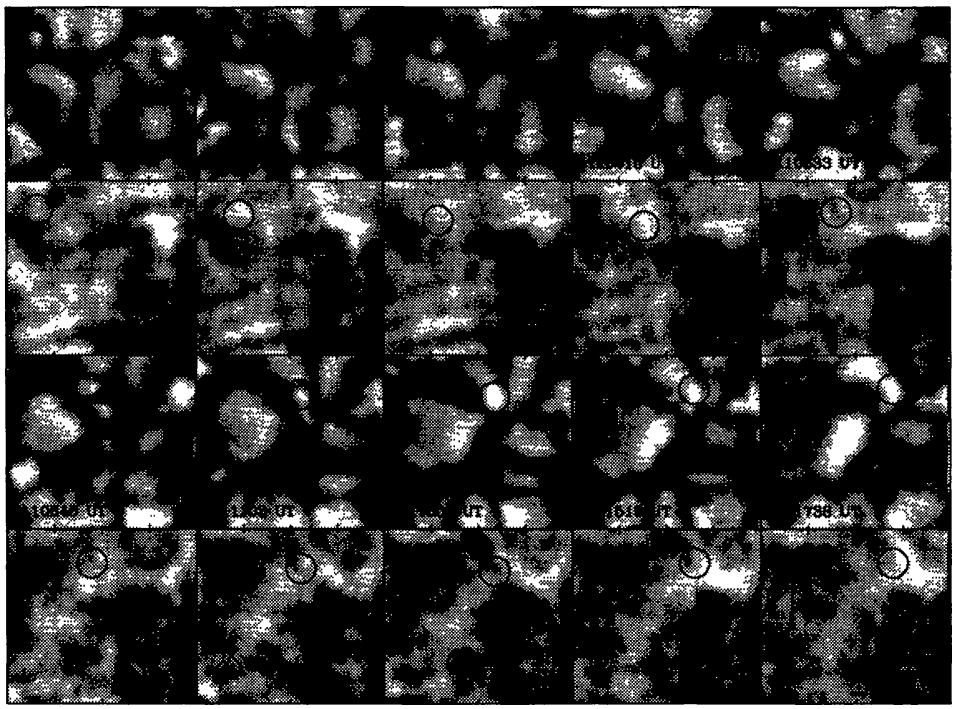

Figure 13: A time series of simultaneous Stokes I and V/I images of a $4''$ by $4''$ field just outside of a penumbra, which is to the left of the field of view. The time increases from the top left to the bottom right and the interval between consecutive images is two minutes. The first and the third rows show Stokes I while the second and the fourth rows show Stokes V/I. The first few magnetograms show signs of remaining fringes. The circle surrounds the position of a moving bright point. Although magnetic fields are found in many places, no significant magnetogram signal can be detected that is cospatial with the bright point.

continuum bright point is located in a magnetic field region, there is no consistent, cospatial magnetic field signal.

Very bright points with more than 50% continuum contrast can be seen in Figs. 14 and 15. The second image has been recorded in almost the same location as the first one, but half an hour later. The bright points are located in a bipolar, emerging active region. The bright points are relatively large, i.e. have diameters of up to 300 km, but they are not always cospatial with the strongest flux concentrations, although they are always close to such locations. It is very likely that these are not bright points as discussed above but some other phenomenon associated with magnetic fields. I may just speculate on their origin: line weakening in the rather temperature sensitive Fe I 525.02 nm line might strongly reduce the Stokes V/I_c signal in the bright and therefore hot points, the field might be strongly inclined, which is not unexpected in an emerging, bipolar region, or it might be a combination of these effects. The current observations do not give a hand on deciding which explanation is correct. Furthermore, it might be

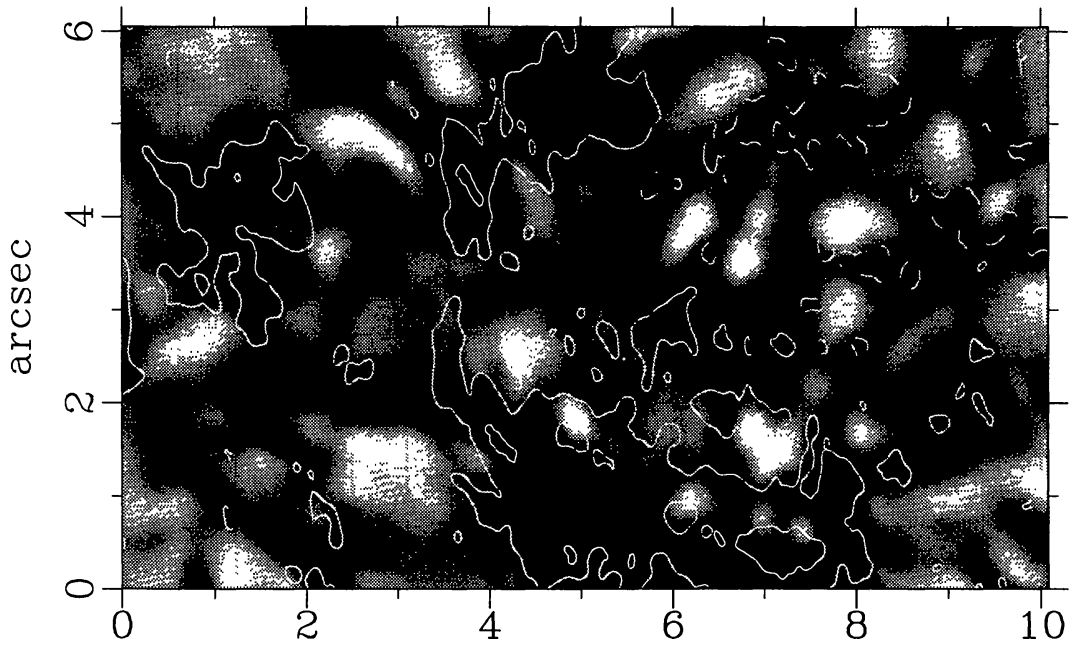

Figure 14: Part of a bipolar, emerging active region at $\mu = 0.94$. Many continuum bright points are brighter by more than 50% than the average quiet Sun brightness and are not always cospatial with strong magnetic signals. Contour lines are drawn at a Stokes V/I_c signal level of 6%. Dashed contour lines indicate the opposite polarity.

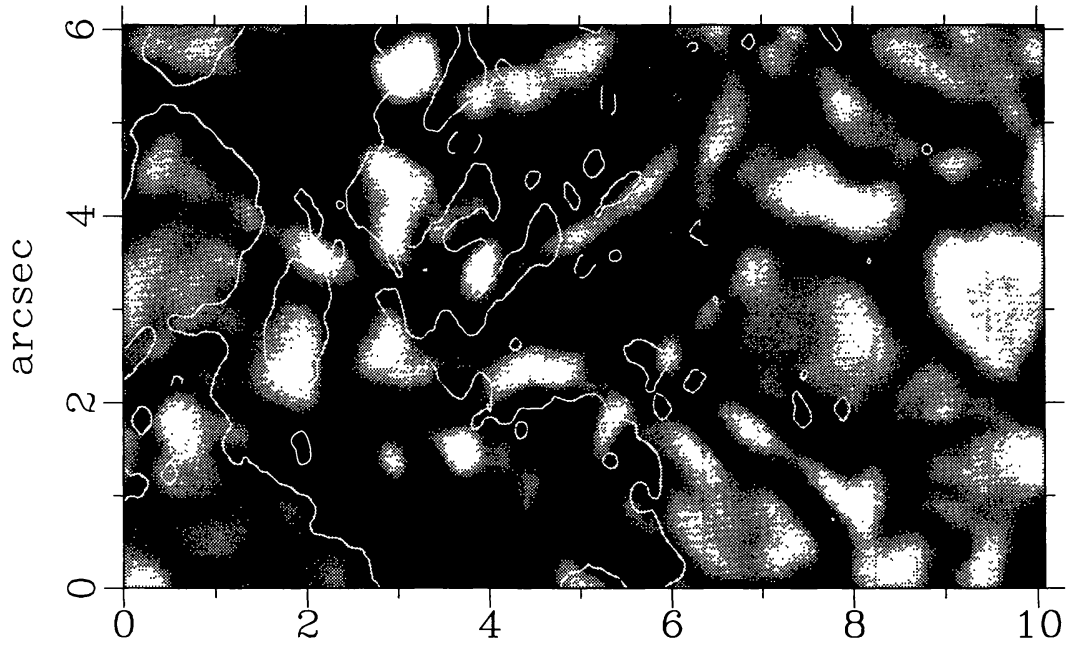

Figure 15: The same emerging active region at $\mu = 0.94$ as in Fig. 14, but 28 minutes later.

an intrinsic magneto-convective phenomenon such as the quenching of up-flowing, non-magnetic gas surrounded by magnetic fields.

Figure 15 also shows very elongated bright and dark structures roughly in the center of the image that are directed from the lower left to the upper right. Comparison with Fig. 14 shows that these structures extend between regions of opposite polarities. These may be the signatures of emerging flux loops as has been suggested by e.g. Bray and Loughhead (1964).

Even in relatively quiet regions, small granules with diameters of 400–600 km with continuum contrasts up to 40% may be seen that have no associated magnetic signal (e.g., the granule to the right of "c" in Fig. 3). Bright small granules near magnetic areas might have been detected in previous observations. In 45% of the cases, Steshenko (1968) was not able to detect a magnetic field in facular granules with sizes of 1.5–3″.

5 Pores

Whereas sunspots and magnetic elements have been investigated in detail by numerous observers, only a limited number of observations of pores and theoretical models exist. Due to their size and restricted lifetime they are not as easy to observe as sunspots. The differentiation between small sunspots and pores is somewhat arbitrary. Often (e.g. Bray & Loughhead 1964) pores are defined as spots having no penumbral structures, i.e. elongated, filament-like bright and dark structures around a central dark core.

It has recently been suggested that the magnetic field of small pores extends beyond the dark umbra (Zirin & Wang 1992). All pores whose images have been reconstructed with solar speckle polarimetry show that the magnetic field covers an area larger than the dark area (see the lower panel of Fig. 16). In this surrounding magnetic field, the pores often show radially elongated structures similar to penumbral filaments in sunspots (see the upper panel of Fig. 16). In the example shown in Fig. 16 the length of these filaments is about 0.″5 to 1″, the separation between them is about 0.″3 to 0.″5, and the brightness of bright filaments is about 1.0–1.1 while that of the dark filaments is about 0.9–1.0 times the average quiet Sun brightness. Some pores show extended magnetic fields that are in regions that are generally darker than the quiet Sun. Figure 17 shows a large pore with an extended, irregularly shaped magnetic field. Note the bright structure close to the pore that has a maximum contrast of 43%.

The pore labeled "h" in Fig. 4 has an umbral dot, which shows average quiet Sun brightness. This is not an uncommon feature. Figure 18 shows a large pore close to a sunspot penumbra that is virtually filled with umbral dots whose brightness distribution is very broad and ranges up to quiet Sun brightness levels.

6 Discussion

It has been shown that speckle deconvolution is an excellent method to obtain nearly diffraction limited narrow-band images with an arbitrarily large field of view. The application of the speckle deconvolution technique to polarimetric observations

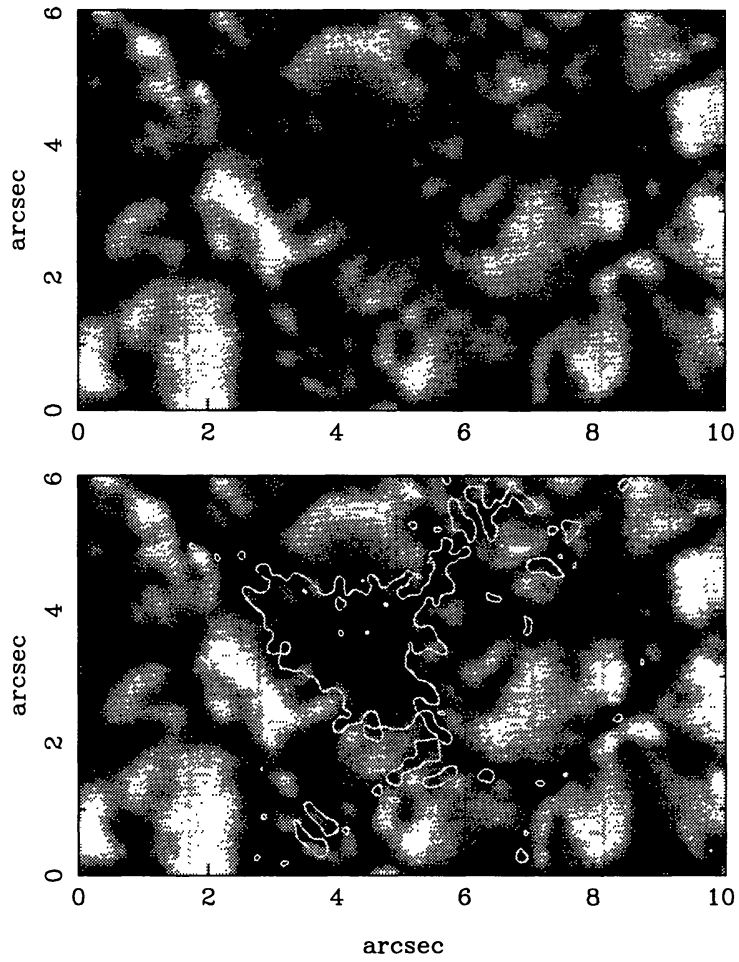

Figure 16: Both panels show the same small pore near disk center in the continuum. The contour lines of the Stokes V/I_c signal at 4% are overlaid on the lower panel. The magnetic field of the pore extends well beyond the dark umbra of the pore. The upper panel shows penumbral filament like structures within the extended magnetic field.

of the solar magnetic field gave new insight into the small-scale structures of magnetic fields in the solar photosphere. New detector systems will provide a better SNR for the polarization measurement and larger telescopes will certainly increase the spatial resolution. ZIMPOL I, the first Zurich Imaging Stokes Polarimeter (Keller et al. 1992) has recently become operational. This novel instrument can simultaneously record up to 10 frames per second of all 4 Stokes parameters or one Stokes parameter in 3 different wavelength regions as well as a broad-band channel. It combines the advantages of a speckle imaging system and a highly sensitivity polarimeter. Techniques such as speckle imaging and speckle spectrography suggest that large, future solar telescopes may deliver high spatial resolution narrow-band images even without adaptive optics. It will be hard to much improve the resolution and the SNR of the present work with existing solar telescopes. The need for a large, polarization free telescope at a good site grows stronger and stronger. The Large Earth-based Solar Telescope (Engvold & Andersen 1990) is an excellent example of such a design to obtain a sound understanding of small-scale solar structures.

Speckle polarimetry shows solar magnetic fields at a spatial resolution that can hardly be achieved with conventional techniques. An important finding due to this new method is the direct resolution of magnetic fluxtubes (Keller 1992). It

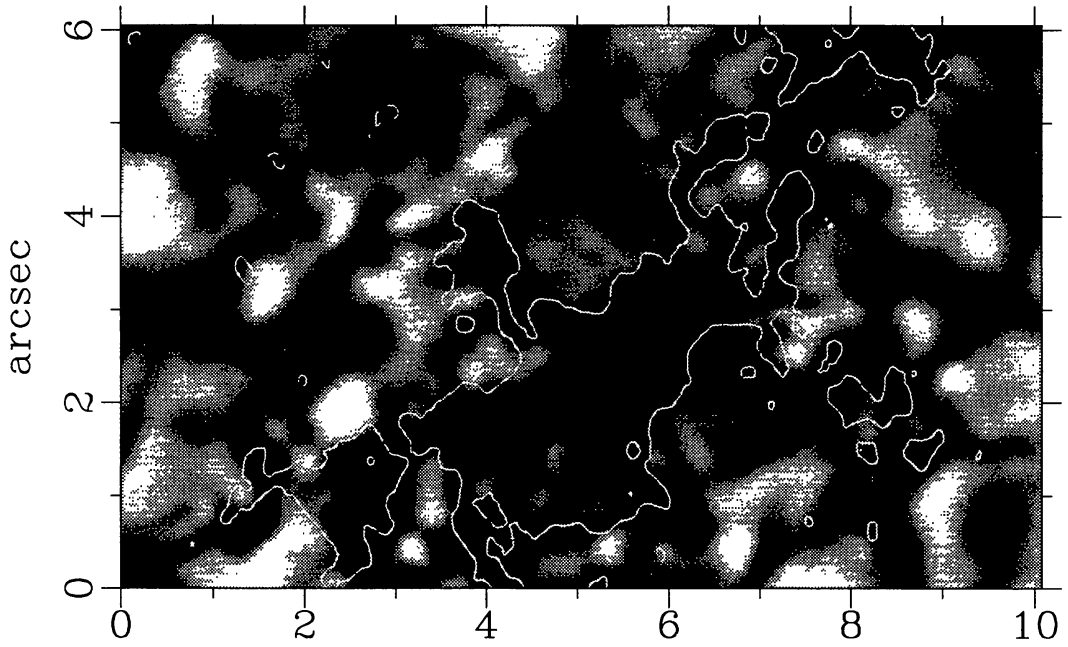

Figure 17: Another pore showing extended magnetic fields. Note the highly structured boundary.

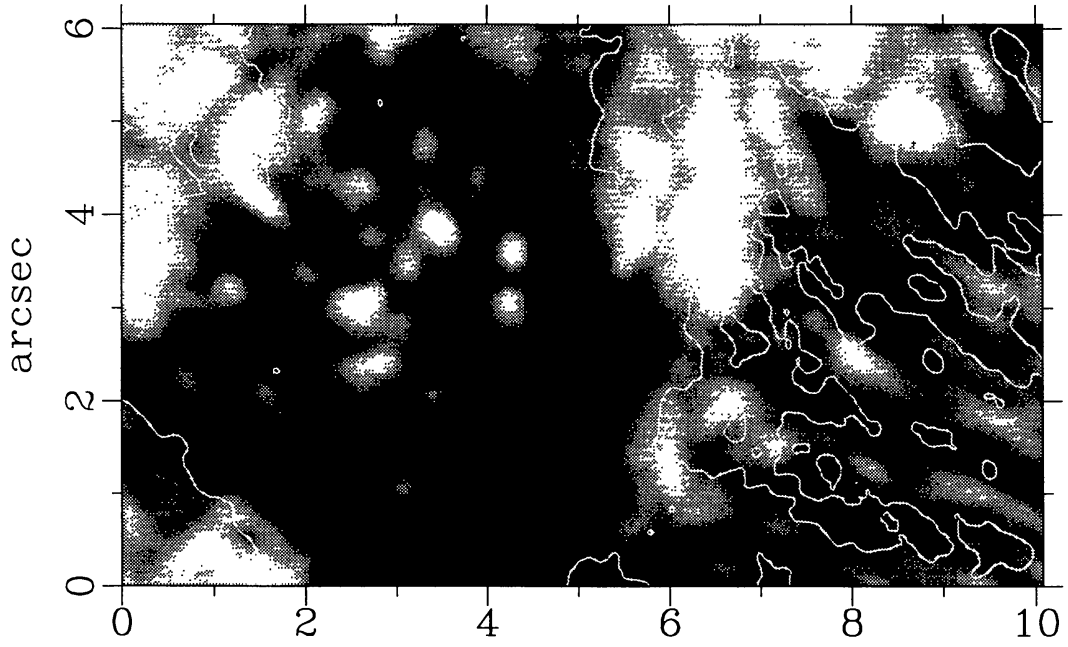

Figure 18: A large pore filled with umbral dots. A part of a sunspot penumbra can be seen to the right. Contour lines indicate the regions with the strongest Stokes V/I_c signal. Since magnetic fields in a sunspot penumbra are almost horizontal, their circular polarization signal is weak.

has been shown that there exist bright points with cospatial strong magnetic fields, although they seem to be rare. The continuum contrast is similar to that of network bright points (Muller & Keil 1983). In general, the observed characteristics of these magnetic elements are compatible with values predicted by indirect observations (e.g. Solanki 1990) and theoretical models (Schüssler 1990) of fluxtubes. There is a distribution of sizes that extends from small bright to larger dark features, which is in agreement with earlier observations and theoretical investigations (e.g. Spruit & Zwaan 1981, Knölker & Schüssler 1988, Title et al. 1992, Topka et al. 1992). The transition from bright to dark elements occurs at an extension of about 300 km in at least one dimension. Theoretical models estimated that the transition occurs at about 500 km (Knölker & Schüssler 1988), which is in reasonable agreement. The properties of larger, dark elements are similar to magnetic knots (Beckers & Schröter 1968) and micro-pores (Zirin & Wang 1992). Elements with particularly strong magnetic signals are often in non-bright regions (Title et al. 1992, Topka et al. 1992), which is now also deduced from a careful analysis of Fourier transform spectrometer data (Solanki & Brigljević 1992). In weaker plages most of the flux is in regions that have about the same intensity distribution as the non-magnetic photosphere. Only the pixels with the strongest magnetic signals are darker than the average brightness. This might be due to the high temperature sensitivity of the spectral line used in this work, which produces enhanced polarization signals at a constant field strength when the temperature is reduced. The continuum brightness of magnetic elements in even less magnetic regions (e.g. in the network) needs to be studied.

Some observations suggested that the magnetic field occupies a much larger area than the bright structures (e.g. Simon & Zirker 1974, Koutchmy & Stellmacher 1978). The present observations show small, bright points that may be classified as continuum bright points, but their magnetic field signal does not significantly extend beyond the bright region. The earlier observations had lower spatial resolution of the magnetic field data as compared with the continuum data, which might explain the discrepancy. It is even more likely that the observations cited above refer to dark magnetic elements where bright internal structures are not well correlated with the magnetic field signature. Since the diameter of the elements is often close to the diffraction limit of the telescope, no reliable result on the shape can be obtained from the present observations. The larger elements, however, often show relatively complicated shapes. When elements are separated by a distance that is close to the diffraction limit, they become hard to distinguish from a single, elongated element.

There remains the question whether there are many magnetic elements close to disk center that are really darker than the average brightness. Indeed, I checked whether I could detect point-like features in the continuum that are brighter than their surrounding, but not necessarily brighter than the average quiet Sun. While such features certainly exist, it is not a very common phenomenon. The polarization signal is detected on a more or less polarization-free background. The intensity is observed in a jungle of bright granules and dark intergranular lanes. Magnetic elements are exclusively located outside of regular granules. It might therefore be the case that I am able to see a concentrated polarization signal while the associated bright point becomes indiscernible due to the limited resolution. However, the flux

regions indicated by the contour lines correspond to densities of the magnetic flux of about 50% of a fully resolved magnetic fluxtube. If a bright structure of say 30% contrast is cospatial with the polarization signal, then a brightness excess of about 10% may surely be expected and would be easy to detect.

I have shown an example of a magnetic element evolving significantly within 16 minutes, similar to the time scale associated with bright points (e.g. Dunn and Zirker 1973, Muller 1983). Evolution on a similar time scale has also been seen by Title et al. (1990), although their observations indicate that the magnetic flux appears and disappears on a much longer time scale.

Plage regions show the familiar pattern of abnormal granulation (Dunn & Zirker 1973). There are no regular granules within highly magnetic regions, but normal granules may be found just adjacent to these magnetic areas. As seen at the high spatial resolution provided by speckle imaging techniques, the abnormal granulation in highly magnetic regions cannot be adequately described by small granules or points embedded in a net of darker lanes (e.g. Muller 1989, Title et al. 1990); it is probably more adequate to say that there is no morphological difference between bright and dark features at the present spatial resolution.

The fast moving bright point without significant magnetic signal is a puzzle. Its long lifetime, size, and brightness suggest that it is not just a bright granule fragment, but an entity that moves through the evolving granulation. If it is associated with concentrated magnetic fields, the corresponding fluxtube must be strongly inclined, which would result in a weak magnetogram signal. However, since the point is moving away from the bipolar region, a particular reason for a strong inclination is not obvious. A strong inclination might be expected close to the neutral line between opposite polarities, but the region shown in Fig. 13 is far away from the neutral line. It should be noticed, however, that the point appears in a region of opposite polarities that are mixed on a small scale.

Pores do not show a significant morphological difference with respect to small sunspots, except for the lack of a well developed penumbral structure. It has been shown that pores have magnetic fields extending beyond the dark umbra and short penumbral structures sometimes appear in the extended field region. The magnitude of the magnetic signal outside of the umbral part of the pore cannot be explained by a lower spatial resolution in the simultaneous Stokes V maps, polarized stray-light from the umbra, or by the higher level of formation of the Stokes V signal with respect to the level of continuum formation. Since pores have less flux than sunspots, the spreading of the field lines is not so fast and therefore the fields are more vertical. Therefore the penumbral structure might be very short as compared to sunspot penumbrae. Since there exist pores and sunspots with the same diameter, the magnetic flux alone is probably not the only parameter that determines the formation of a sunspot penumbra. The existence of a penumbra-like structure around most pores might give hints for theoretical studies of penumbrae. In particular, it might render superfluous a postulated critical flux value for the formation of a penumbra (e.g. Schmidt et al. 1986).

Finally, I would like to present observations from a region on the dark backside of the Sun observed on April 1, 1999 (see Fig. 19). The super-resolved umbral dots in two of the pores as well as the lack of a polarization signal in the pores is a complete mystery.

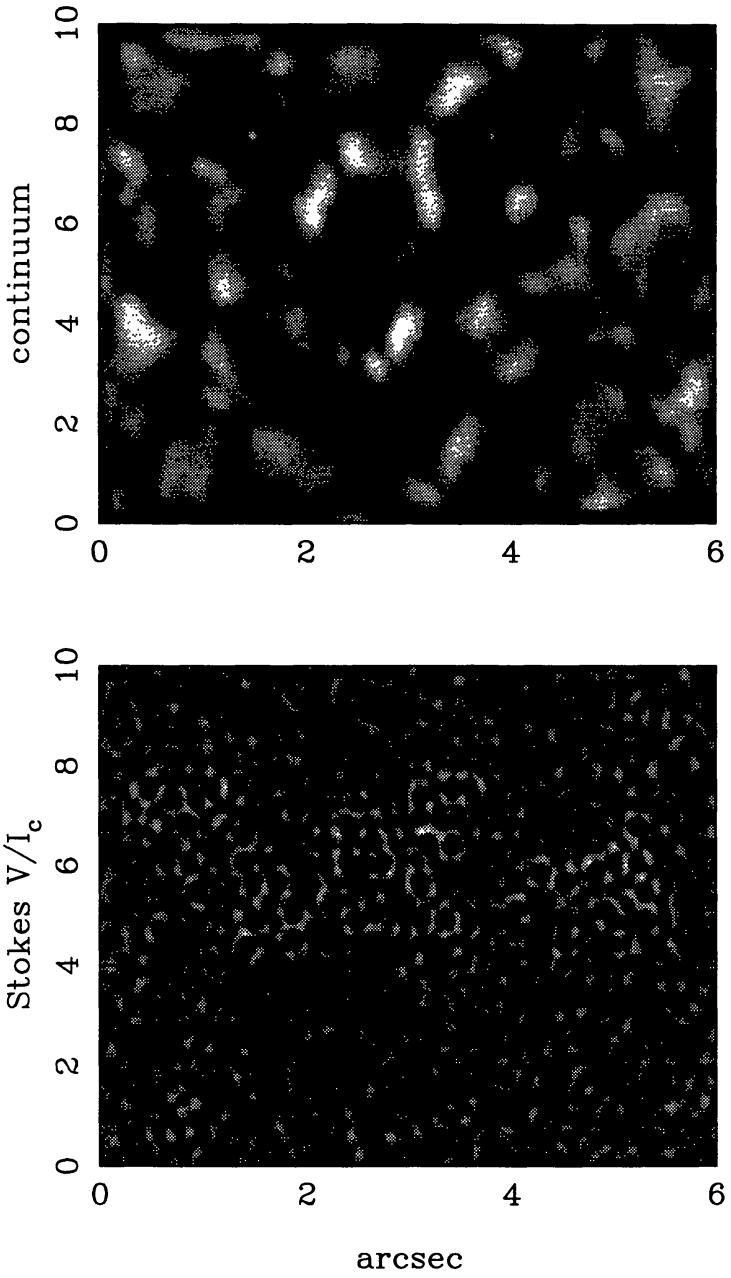

Figure 19: Currently unexplained observation in a pore region. The upper panel shows a cluster of four pores, two of which exhibit umbral dots with apparent diameters well below the diffraction limit. The lower panel shows the magnetic signal in the same area. Numerous magnetic elements are aligned in circles and lines.

Acknowledgements

I am grateful to O. von der Lühe, who introduced me to speckle imaging and made his KISIP program available, to G.B. Scharmer for teaching me how to record high resolution images of the Sun and for assistance during the observations, and to J.O. Stenflo for his continuous support. I also express my gratitude to the Astronomische Gesellschaft for the travel support. This work has been supported by the Swiss National Science Foundation under grant No. 8220-037202. The National Optical Astronomy Observatories are operated by the Association of Universities for Research in Astronomy, Inc. (AURA) under cooperative agreement with the National Science Foundation.

References

Aime C., 1989. In: von der Lühe O. (ed.) Proc. of the Tenth Sacramento Peak Summer Workshop, High Spatial Resolution Solar Observations. New Mexico, p. 127

Aime C., Borgnino J., Druesne P., Harvey J.W., Martin F., Ricort G., 1985. In: Muller R. (ed.) High Resolution in Solar Physics. Lecture Notes in Physics 233, Springer, Berlin, p. 103

Auffret H., Muller R., 1991, A&A 246, 264

Beckers J.M., 1982, Optica Acta 29, 361

Beckers J.M., 1989. In: Rutten R.J., Severino G. (eds.) Solar and Stellar Granulation. Kluwer, Dordrecht, p. 55

Beckers J.M., Schröter E.-H., 1968, Solar Phys. 4, 142

Biermann L., 1941, Vierteljahrssch. Astr. Gesellsch. 76, 194

Brault J.W., White O.R., 1971, A&A 13, 169

Bray R.J., Loughhead R.E., 1964, Sunspots. The Int. Astrophys. Ser. VII, Chapman and Hall, London

Choudhuri A.R., Auffret H., Priest E.R., 1993, Solar Phys. 143, 49

Christou J.C., Ribak E., Hege E.K., Freeman J.D., 1986, Opt. Eng. 25, 724

Craig J.D., Brown J.C., 1986, Inverse Problems in Astronomy. Adam Hilger Ltd, Bristol, Great Britain

Daubechies I., 1988, Commun. Pure and Appl. Math. 41, 909

de Boer C.R., Kneer F., 1992, A&A 264, L24

de Boer C.R., Kneer F., Nesis A., 1992, A&A 257, L4

Dunn R.B., Zirker J.B., 1973, Solar Phys. 33, 281

Engvold O., Andersen T., 1990, Status of the Design of the Large Earth-based Solar Telescope. LEST Foundation

Fontanella J.C., Primot J., 1987. In: Goad J.W. (ed.) Interferometric Imaging in Astronomy. ESO/NOAO, Oracle, Arizona, p. 209

Frank Z.A., Scharmer G.B., Keller C.U., Lundstedt H., 1991, BAAS 23, 1052

Fried D.L., 1966, J. Opt. Soc. Am. 56, 1372

Hale G.E., 1908, ApJ 28, 315

Harvey J.W., Livingston W.C., 1969, Solar Phys. 10, 283

Harvey J.W., 1986. In: Deinzer W., Knölker M., Voigt H.H. (eds.) Small Scale Magnetic Flux Concentrations in the Solar Photosphere. Vandenhoeck and Ruprecht, Göttingen, p. 25

Hebden J.C., Hege E.K., Beckers J.M., 1986, Opt. Eng. 25, 712

Hénoux J.C., Somov B.V., 1991, A&A 241, 613

Keller C.U., 1992, Nature 359, 307

Keller C.U., 1993a. In: Zirin H., Ai G., Wang H. (eds.) IAU Coll. 141, The Magnetic and Velocity Fields of Solar Active Regions, Astronomical Society of the Pacific Conference Series Vol. 46, San Francisco, California, p. 3

Keller C.U., 1993b. In: Schüssler M., Schmidt W. (eds.) Solar Magnetic Fields. Cambridge University Press, Great Britain, p. 325

Keller C.U., 1994. In: Rutten R.J., Schrijver C.J. (eds.) Solar Surface Magnetism, Kluwer, Dordrecht, p. 43

Keller C.U., Johannesson A., 1995, A&AS in press

Keller C.U., von der Lühe O., 1992a. In: Beckers J.M., Merkle F. (eds.) Proc. of the ESO Conference on High Resolution Imaging by Interferometry II, ESO, p. 453
Keller C.U., von der Lühe O., 1992b, A&A 261, 321
Keller C.U., von der Lühe O., 1994. In: Radick R.R. (ed.) Proc. of the Thirteenth Sacramento Peak Summer Workshop, Real Time and Post-Facto Solar Image Correction. New Mexico, p. 129
Keller C.U., Solanki S.K., Steiner O., Stenflo J.O., 1990, A&A 233, 583
Keller C.U., Aebersold F., Egger U., et al., 1992, LEST Technical Report 53
Knölker M., Schüssler M., 1988, A&A 202, 275
Knox K.T., Thompson B.J., 1974, ApJ 193, L45
Korff D., 1973, J. Opt. Soc. Am. 63, 971
Koutchmy S., Stellmacher G., 1978, A&A 67, 93
Labeyrie A., 1970, A&A 6, 85
Löfdahl M.G., Scharmer G.B., 1994, A&AS 107, 243
Lohmann A.W., Weigelt G., Wirnitzer B., 1983, Applied Optics 22, 337
Lundstedt H., Johannesson A., Scharmer G.B., et al., 1991, Solar Phys. 132, 233
Mehltretter J.P., 1974, Solar Phys. 38, 43
Morlet J., Arens G., Fourgeau E., Giard D., 1982, Geophys. 47, 203
Muller R., 1983, Solar Phys. 85, 113
Muller R., 1985, Solar Phys. 100, 237
Muller R., 1989. In: Rutten R.J., Severino G. (eds.) Solar and Stellar Granulation. Kluwer, Dordrecht, p. 101
Muller R., Keil S.L., 1983, Solar Phys. 87, 243
Muller R., Roudier T., Hulot J.C., 1989, Solar Phys. 119, 229
Pehlemann E., von der Lühe O., A&A 216, 337
Petrov R., Kadiri S., Martin F., Ricort G., Aime C., 1982, J. Opt. (Paris) 13, 331
Petrov R., Roddier F., Aime C., 1986, J. Opt. Soc. Am. A 3, 634
Press W.H., 1991, Harvard-Smithsonian Center for Astrophysics Preprint No. 3184
Primot J., Rousset G., Fontanella J.C., 1990, J. Opt. Soc. Am. A 7, 1598
Ramsey H.E., Schoolman S.A., Title A.M., 1977, ApJ 215, L41
Schatten K.H., Mayr H.G., 1991, ApJ 372, 728
Schüssler M., 1990. In: Stenflo J.O. (ed.) IAU Symp. 138, Solar Photosphere: Structure, Convection, Magnetic Fields. Kluwer, Dordrecht, p. 161
Schmidt H.U., Spruit H.C., Weiss N.O., 1986, A&A 158, 351
Seldin J.H., Paxman R.G., 1994, SPIE Proc. 2302, 268
Semel M., 1987, A&A 178, 257
Shurcliff W.A., 1962, Polarized Light. Harvard University Press, Cambridge
Simon G.W., Zirker J.B., 1974, Solar Phys. 35, 331
Solanki S.K., 1990. In: Stenflo J.O. (ed.) IAU Symp. 138, Solar Photosphere: Structure, Convection, Magnetic Fields. Kluwer, Dordrecht, p. 103
Solanki S.K., 1993, Space Science Rev. 63, 1
Solanki S.K., Brigljević V., 1992, A&A 262, L29
Spruit H.C., Zwaan C., 1981, Solar Phys. 70, 207
Steiner O, 1994. In: Rabin D.M., Jefferies J.T., Lindsey C. (eds.) IAU Symp. 154, Infrared Solar Physics. Kluwer, Dordrecht, p. 407
Stenflo J.O., 1973, Solar Phys. 32, 41

Stenflo J.O., 1989, A&AR 1, 3
Stenflo J.O., 1994, Solar Magnetic Fields: Polarized Radiation Diagnostics. Kluwer Academic Publishers, Dordrecht, The Netherlands
Stenflo J.O., Harvey J.W., Brault J.W., Solanki S.K., 1984, A&A 131, 333
Steshenko N.V., 1968. In: Kiepenheuer K.O. (ed.) IAU Symp. 35, Structure and Development of Solar Active Regions. Reidel, Dordrecht, p. 201
Title A.M., Tarbell T.D., Topka K.P., et al., 1990. In: Russell C.T., Priest E.R., Lee L.C. (eds.) Physics of Magnetic Flux Ropes. Geophysical Monograph 58, p. 171
Title A.M., Topka K.P., Tarbell T.D., et al., 1992, ApJ 393, 782
Title A.M., Frank Z.A., Shine R.A., et al. 1993, ApJ 403, 780
Topka K.P., Tarbell T.D., Title A.M., 1992, ApJ 396, 351
von der Lühe O., 1984, J. Opt. Soc. Am. A 1, 519
von der Lühe O., 1989. In: von der Lühe O. (ed.) Proc. of the Tenth Sacramento Peak Summer Workshop, High Spatial Resolution Solar Observations. New Mexico, p. 147
von der Lühe O., 1992. In: Sánchez F., Collados M., Vázquez M. (eds.) Solar Observations: techniques and interpretation. Cambridge University Press, p. 1
von der Lühe O., 1993, A&A 268, 374
von der Lühe O., 1994, A&A 281, 889
Zirin H., Wang H., 1992, ApJ 385, L27